machines

Article

Dynamic Characteristics, Analysis, and Measurement of a Large Optical Mirror Processing System

Zujin Jin [1], Zixin Yin [1,2,*], Hao Liu [1] and Fuchao Liu [3]

[1] School of Mechanical and Electronic Engineering, Suzhou University, Suzhou 234000, China; jinzj@ahszu.edu.cn (Z.J.); lb20050011@cumt.edu.cn (H.L.)
[2] Suzhou University Technology and Research Center of Engineering Tribology, Suzhou University, Suzhou 234000, China
[3] Shandong Xinsha Monorail Transport Equipment Co., Ltd., Xintai 271200, China; zqf0920@163.com
* Correspondence: yinzixin@ahszu.edu.cn

Abstract: Optical mirrors have high requirements for surface precision, requiring ultra-precision processing. The revolving movement of a computer-controlled optical surfacing (CCOS) grinding system will induce vibrations in a five-degrees-of-freedom hybrid processing robot (5-DOF-HPR) and a flexible support system (FSS) in a large optical mirror processing system (LOMPS). As a result, the mirror surface will vibrate, which will ultimately affect the surface accuracy of the final optical mirror. Therefore, the differential equation representing the vibration of the 5-DOF-HPR is established based on the spatial beam unit, which transforms the generalized coordinates into modal coordinates, thereby removing the coupling terms of the vibration differential under generalized coordinates. At the same time, a dynamic analysis of the CCOS grinding system is performed, and the magnitude and direction of the centrifugal force and reaction force are calculated. Then, the natural frequencies of the 5-DOF-HPR and the FSS are measured experimentally and compared with the simulation results; thus, the accuracy and effectiveness of the model are verified. Finally, the vibration characteristics of the processed optical mirrors under different influencing factors are obtained. A theoretical and experimental basis for parameter optimization and path planning of the LOMPS is provided to improve the surface accuracy of the processed optical mirror.

Keywords: optical mirror processing; elastic dynamics; vibration characteristics; measurement

Citation: Jin, Z.; Yin, Z.; Liu, H.; Liu, F. Dynamic Characteristics, Analysis, and Measurement of a Large Optical Mirror Processing System. *Machines* **2024**, *12*, 788. https://doi.org/10.3390/machines12110788

Academic Editor: Yuwen Sun

Received: 26 September 2024
Revised: 31 October 2024
Accepted: 5 November 2024
Published: 7 November 2024

1. Introduction

With the help of evolving technology, modern optical mirrors are being developed with larger apertures and higher precision, among which free-form optical mirrors are widely used. Therefore, a large optical mirror processing system (LOMPS) that is suitable for large sizes, aspherical, high-efficiency, and precise delivery is an urgent technological need. To address this, a LOMPS was designed, which consisted of three heterogeneous robots: a five-degrees-of-freedom hybrid processing robot (5-DOF-HPR), a flexible support system (FSS), and a computer-controlled optical surfacing (CCOS) grinding system. The 5-DOF-HPR can drive the CCOS grinding system to the processing position; the FSS grinding system can adjust the position and posture of the supported optical mirror, and as the support stiffness is adjustable, the CCOS grinding system can perform real-time adjustment of speed and polishing pressure [1]. The four processing steps of the mirror surface—rough grinding, milling, fine grinding, and polishing—can be completed by the LOMPS [2,3]. As the three robots collaborate, the task allocation, path planning, spatial orientation, multiple disturbance mechanisms, and instantaneous dynamic characteristics of each robot vary [4,5]. In particular, in terms of vibration characteristics, because the CCOS grinding system uses a double planetary rotation structure, the revolution of the object generates periodic loads on the parallel robot and optical mirror, and resonance may occur, thereby affecting the surface accuracy of the optical mirror surface [6]. Therefore, it is necessary to analyze the dynamic characteristics of the LOMPS, predict the vibration and deformation trends of the processing system, and avoid resonance. This approach mitigates errors induced by the processing system vibrations, thereby enhancing processing efficiency, surface quality, and geometric precision of the optical mirror [7].

In recent years, many scholars have conducted analyses and research on the dynamic characteristics of different types of robots. To improve the productivity rate without any loss of positioning accuracy, Ariano et al. studied the vibration behavior of industrial manipulator Racer-7-1.4 to reduce its residual vibration and execution time [8]. Hwang et al. established a precise dynamic model of a cable-driven parallel robot under constrained conditions and obtained the natural frequency relative to the position of the end effector, which provided a favorable understanding for the establishment of a vibration suppression scheme [9]. Zhang et al. studied the problem of residual vibration caused by the joint flexibility of a 6-DOF industrial robot and proposed an adaptive input shaping method to suppress the residual vibration [10]. To study the natural frequency and vibration characteristics of the manipulator under the impact of collision, Min et al. proposed a method for estimating the vibration mode of the manipulator structure based on the peak frequency [11]. Yoon et al. proposed a method to reduce the residual vibration of a manipulated object by optimizing the acceleration/deceleration time using the object's natural frequency [12]. Based on the Stewart platform, Wu et al. discussed the effects of strut masses and payload on the natural frequency and dynamic isotropy index, and optimized vibration isolation [13]. Yang et al. formulated a fourth-order periodic time-varying nonlinear dynamic equation for a spin spherical capsule robot subjected to complex external torque utilizing Euler dynamics principles. The dynamic characteristics of the robot were subsequently validated through experimental investigations [14].

Many scholars have tested different research methods when analyzing the dynamic characteristics of robots with different configurations. Tang et al. conducted an analysis of the influence of robot posture on the dynamic flexibility of the end effector based on the robot's end effector relative dynamic compliance index. This research provides theoretical guidance for enhancing the vibration resistance and dynamic performance of traditional cleaning robots [15]. Hoevenaars et al. presented a novel natural frequency analysis method for parallel manipulators that focused on the lowest natural frequencies and expressed the corresponding eigenmodes in an end effector Cartesian reference frame [16]. Ma et al. used operator algebra to derive the equation of motion required to study the dynamics of a space manipulator [17]. Wu et al. used a variety of techniques to modify the finite element model, and the results showed that the improved model could predict the vibration characteristics of an experimental crane with satisfactory accuracy [18]. Nguyen et al. presented a Gaussian process, regression-based approach to model the dynamic properties of a 6-DOF industrial robot within its workspace in order to determine the discrete sampling modal parameters of the robot structure through an experimental modal analysis and accurately predict its modal parameters at different points in the workspace [19]. Ganesh et al. used the stiffness matrix and dynamic mass matrix to obtain the natural frequency and global natural frequency index of a parallel machine tool [20]. Dong et al. proposed a semi-analytical method for robot elastic dynamics based on the screw theory to calculate low-order natural frequencies and vibration shapes and achieved good results [21].

A support cylinder was used as the support element in the FSS. Owing to the different working principles of mechanical–electric industrial robots, the above dynamic characteristics research methods were not suitable. Therefore, many scholars have conducted extensive research on the dynamic characteristics of hydraulic systems. Yang et al. calculated the natural frequency of the robot legs throughout the entire motion cycle of the robot. With the goal of increasing the natural frequency, the leg structure of the robot was optimized [22]. Li et al. analyzed the natural frequency and vibration mode of a hydraulic demolition robot using the finite element method. The optimized design of the prototype provided a theoretical basis and reference for our experimental mode [23]. Guan et al. analyzed the dynamic response characteristics and natural frequencies of a column hydraulic cylinder and balance hydraulic cylinder and improved the structural parameters to increase their natural frequency [24]. Lin et al. conducted an analysis of the impact of structural parameters on the high- and low-frequency dynamic characteristics of a novel bell plate hydraulic suspension system. They compared the influence of varying numbers of bell plates on the dynamic performance of hydraulic supports across different frequency ranges [25]. To investigate the dynamic operational characteristics of hydraulic support lifting, Xie et al. established a rigid flexible coupling dynamic simulation model of the hydraulic support system. They subsequently collected and analyzed the operational characteristic parameters of the hydraulic support [26]. Xu et al. proposed a less modified measurement scheme to accurately obtain the dynamic characteristics of the cylinder block and analyzed its dynamic characteristics under different working pressures [27]. Tao et al. conducted an independent impedance analysis of various structures within magnetostrictive electro-hydraulic actuators, the natural frequencies and dynamic characteristics of manifolds, hydraulic cylinders, and accumulators. Their findings provide theoretical guidance for optimizing the structure and performance of these actuators [28].

The above scholars analyzed the natural frequency, vibration suppression, and modal information of parallel machine tools, hydraulic systems, and industrial robots through different methods and achieved significant results. However, their research focused on a single robot: there was no in-depth research on a system composed of multiple heterogeneous robots. In addition, the external excitations provided during most of the modal test analyses were only artificial vibration excitations in the laboratory environment, and the respective dynamic characteristics of the robots during the working process were not used as influencing factors for the disturbance analysis of multirobot systems. In practical applications, there has been no analysis or research on the vibration characteristics of the workpiece to be processed. However, optical mirrors require high surface accuracy, and the mirror material is brittle. These factors may affect the surface accuracy of the optical mirror and even cause the mirror surface to be scrapped because of excessive vibration during processing. Therefore, modal analyses and experiments on the LOMPS will significantly advance large optical mirror processing.

In this study, the dynamic characteristics of the LOMPS, which is composed of three heterogeneous robots, namely a 5-DOF-HPR, FSS, and CCOS grinding system, were studied and analyzed. First, the vibration differential equation of the 5-DOF-HPR was established based on the spatial beam unit. Then, combined with the finite element method, the vibration model of the FSS was established. At the same time, a dynamic analysis of the revolution of the CCOS grinding system was performed, and the magnitude and direction of the centrifugal force and reaction force under the generalized coordinates were calculated. Then, the natural frequencies of the 5-DOF-HPR and FSS were measured experimentally and compared with the simulation results, and the accuracy and effectiveness of the model were verified. Finally, the amplitudes of the processed optical mirrors at different operating speeds of the 5-DOF-HPR, different support heights of the FSS, and different revolution speeds of the CCOS grinding system were measured, and the vibration characteristics of the processed optical mirrors under different influencing factors were obtained. The proposed method provided a theoretical basis for analyzing the vibration characteristics of the LOMPS and improving the surface accuracy of the processed mirror. It also provided an experimental basis for research on the dynamic characteristics of a machining system composed of multiple heterogeneous robots, such as machine–electro-hydraulic collaborative work. At the same time, it also provided a research basis for the feasibility of precision machining of multiconfiguration robots in complex disturbance environments.

2. Composition of the LOMPS

The 5-DOF-HPR drives the CCOS grinding system to the processing position. The support stiffness of the FSS is adjustable, and the CCOS grinding system can adjust the grinding speed, eccentricity, and polishing pressure. The topology of the LOMPS is shown in Figure 1. The effective operational envelope of the engineered machining robot is a truncated cylinder with a base radius of 815 mm, a minimum height of 200 mm on the Z-axis, and a maximum height of 1250 mm on the Z-axis. The flexible hydraulic support system can accommodate optical mirrors with a maximum diameter of 1250 mm, and the support height can be adjusted within a range of -1 mm to 1 mm.

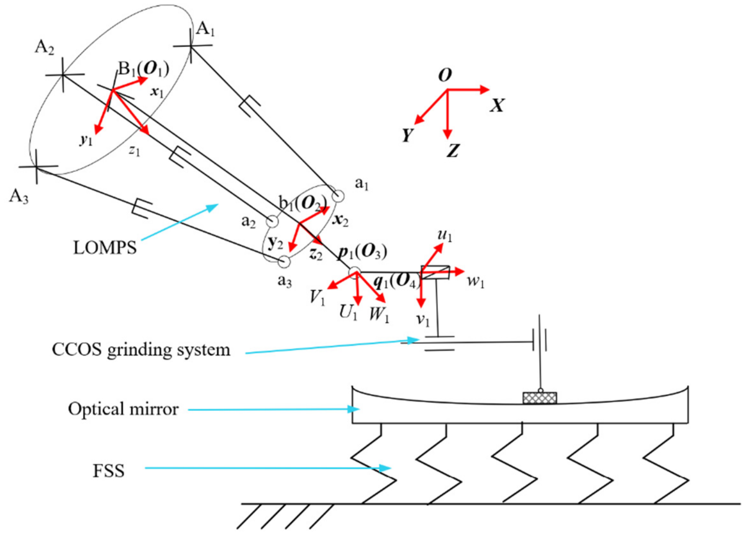

Figure 1. Topological structure of the LOMPS.

2.1. 5-DOF-HPR

During processing, the grinding head must be capable of reaching any position with any attitude. As a result the robot required at least 5 DOF. The 5-DOF robot is composed of a 3-DOF parallel manipulator and a 2-DOF series manipulator.

Establish a fixed coordinate system O_1-$x_1y_1z_1$ and a moving coordinate system O_2-$x_2y_2z_2$ on the center points of the fixed platform and the moving platform respectively. O_1 and O_2 are the origin; y_1 points to O_1A$_3$; z_1 points to O_1 O_2; and z_1 and y_2 follow the right-hand rule.

The conjoined coordinate systems of the two rotating heads are established, and the conjoined coordinate system of the first rotating head is O_3-$U_1V_1W_1$, where O_3 is at intersection point P_1 of the first and second rotating heads. The direction of the W_1-axis points to O_2O_3; the U_1-axis is collinear with the axis of the secondary rotating shaft; and the V_1-axis follows the right-hand rule. The fixed coordinate system O_4-$u_1v_1w_1$ of the secondary rotating head is established at the connection point between the secondary rotating head and the CCOS grinding system, where the w_1-axis and O_3O_4 are collinear, v_1 is collinear with the rotation axis of the secondary rotating shaft, and the u_1-axis follows the right-hand rule.

2.2. FSS

The support point of the FSS was supported by a diaphragm cylinder, which is simplified as a support spring in Figure 1. The structure and distribution of the diaphragm cylinder are shown in Figure 2. The large and small diaphragms make the support cylinder form two chambers, and the beryllium bronze reed restricts the swing of the support shaft. As shown in Figure 3, the 36 cylinders were divided into three sectors. The support height and rigidity of the support cylinder could be controlled; thus, the posture of the optical mirror could be adjusted.

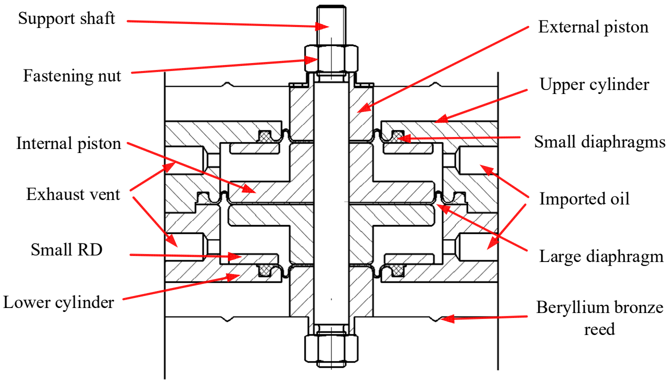

Figure 2. Structure of diaphragm cylinder.

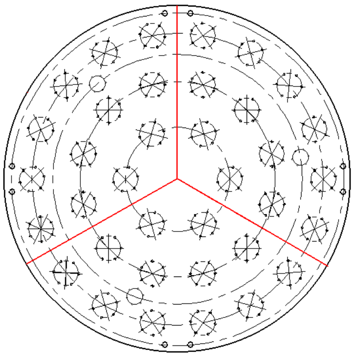

Figure 3. Arrangement diagram of support cylinders.

2.3. CCOS Grinding System

The CCOS grinding system consisted of two motors: a revolution motor and a rotation motor. The rotation motor was eccentrically arranged relative to the revolution motor, and the distance between the axis of the two motors could be adjusted using an eccentric adjustment device. The rotation motor was connected to the grinding disc through a pneumatic pressure device, and the air pressure can be adjusted. Through the Preston equation, the relationship between the speed and pressure and the removal amount is:

$$\frac{dz}{dt} = KVP \tag{1}$$

where K is a proportional constant, V is the polishing speed, P is the positive pressure. And the removal amount Δz of the surface material of a processing element, as shown in Equation (2).

$$\Delta z(x, y) = K \int V(x, y, t) P(x, y) dt \tag{2}$$

3. Dynamic Characteristic Analysis of LOMPS

During the operation of the LOMPS, the robots affected each other. As these three robots had different configurations, their dynamic characteristics were also completely different. Therefore, it was also necessary to analyze the three robots separately during the dynamic analysis process.

3.1. Dynamic Characteristic Analysis of the 5-DOF-HPR

3.1.1. Element Division and Establishment of Element Dynamics

When a beam in space is deformed, the component elements of the beam are forced to undergo deformation. Here, the j-th unit model on the i-th branch was selected for analysis. A model of the spatial beam element is shown in Figure 4.

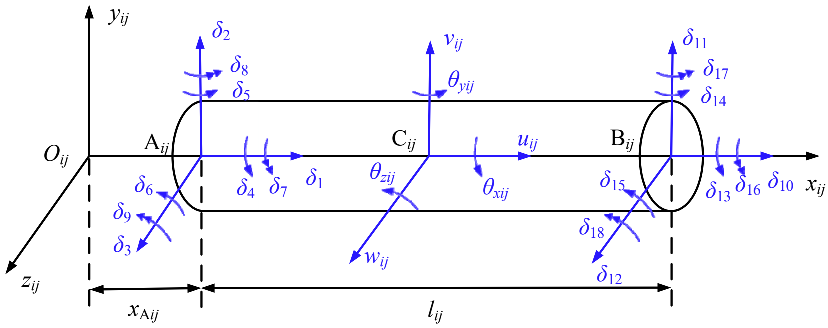

Figure 4. Generalized coordinates of beam element.

The element coordinate system O_{ij}-$x_{ij}y_{ij}z_{ij}$ on the element node was established, and the element coordinate system coincided with the branch chain coordinate system. $\delta = [\delta_1, \delta_2, \cdots, \delta_{18}]^{\mathrm{T}}$ was used as the generalized coordinate vector for the beam element. Among them, δ_1–δ_3 and δ_{10}–δ_{12} represented the elastic displacements of the element nodes along the x_{ij}-, y_{ij}-, and z_{ij}-axes; δ_4–δ_6 and δ_{13}–δ_{15} represented the elastic rotation angles of the element nodes along the x_{ij}-, y_{ij}-, and z_{ij}-axes, and δ_7–δ_9 and δ_{16}–δ_{18} represented the curvature of the element nodes.

The unit kinetic energy T and the unit variable performance V are respectively,

$$\boldsymbol{T} = \frac{1}{2}(\dot{\delta}_r + \dot{\delta})^{\mathrm{T}} \boldsymbol{M}_e (\dot{\delta}_r + \dot{\delta}) \tag{3}$$

$$\boldsymbol{V} = \frac{1}{2}\delta^{\mathrm{T}} \boldsymbol{K}_e \delta \tag{4}$$

where $\dot{\delta} = [\dot{\delta}_1 \quad \cdots \quad \dot{\delta}_{18}]$, $\boldsymbol{M}_e$ is the element mass matrix, $\boldsymbol{K}_e$ is the element stiffness matrix, $\dot{\delta}_r = [\dot{x}_{Aij} \quad \dot{y}_{Aij} \quad \dot{z}_{Aij} \quad \dot{\theta}_x \quad \dot{\theta}_y \quad \dot{\theta}_z \quad 0 \quad 0 \quad 0 \quad \dot{x}_{Bij} \quad \dot{y}_{Bij} \quad \dot{z}_{Bij} \quad \dot{\theta}_x \quad \dot{\theta}_y \dot{\theta}_z \quad 0 \quad 0 \quad 0]$, $\dot{x}_{Aij}$, $\dot{y}_{Aij}$, and $\dot{z}_{Aij}$ are the rigid body velocities along the x-, y-, and z-axes at the cell node A_{ij}, respectively; $\dot{x}_{Bij}$, $\dot{y}_{Bij}$, and $\dot{z}_{Bij}$ are the rigid body velocities along the x-, y-, and z-axes at the cell node B_{ij}, respectively; and $\dot{\theta}_x$, $\dot{\theta}_y$, and $\dot{\theta}_z$ are the rigid body angular velocities along the x-, y-, and z-axes at the cell node A_{ij}, respectively.

From the Lagrange equation,

$$\frac{d}{dt}\left(\frac{\partial T}{\partial \dot{\delta}}\right) - \frac{\partial T}{\partial \delta} + \frac{\partial V}{\partial \delta} = \boldsymbol{F} \tag{5}$$

The dynamic equation of the element is obtained.

$$\boldsymbol{M}_e \ddot{\delta} + \boldsymbol{C}_e \dot{\delta} + \boldsymbol{K}_e \delta = \boldsymbol{F}_e + \boldsymbol{P}_e + \boldsymbol{Q}_e \tag{6}$$

where $\boldsymbol{C}_e$ is the element damping matrix, $\boldsymbol{F}_e$ is the element generalized external force (including force and moment), $\boldsymbol{P}_e$ is the force between beam elements, and $\boldsymbol{Q}_e$ is the rigid body inertial force array of the system element.

The transformation matrix $\overline{\boldsymbol{R}}_{ij}$ from the element coordinate system to the fixed coordinate system is introduced, and the elastic dynamic equation of the element in the fixed coordinate system is obtained.

$$\overline{\boldsymbol{M}}_{ij} \ddot{\overline{\delta}}_{ij} + \overline{\boldsymbol{C}}_{ij} \dot{\overline{\delta}}_{ij} + \overline{\boldsymbol{K}}_{ij} \delta_{ij} = \overline{\boldsymbol{Q}}_{ij} \tag{7}$$

where, $\overline{\boldsymbol{M}}_{ij} = \overline{\boldsymbol{R}}_{ij}^{\mathrm{T}} \boldsymbol{M}_e \overline{\boldsymbol{R}}_{ij}$, $\overline{\boldsymbol{K}}_{ij} = \overline{\boldsymbol{R}}_{ij}^{\mathrm{T}} \boldsymbol{K}_e \overline{\boldsymbol{R}}_{ij}$, $\overline{\boldsymbol{C}}_{ij} = \lambda_1 \overline{\boldsymbol{M}}_{ij} + \lambda_2 \overline{\boldsymbol{K}}_{ij}$, and $\overline{\boldsymbol{Q}}_{ij} = \overline{\boldsymbol{R}}_{ij}^{\mathrm{T}} \boldsymbol{F}_e + \overline{\boldsymbol{R}}_{ij}^{\mathrm{T}} \boldsymbol{P}_e + \overline{\boldsymbol{R}}_{ij}^{\mathrm{T}} \boldsymbol{Q}_e$.

3.1.2. Elastic Dynamic Analysis of UPS Branch Chain

As shown in Figure 5, the UPS branch chain can be regarded as composed of a swing rod, telescopic rod, and composite ball hinge. The swing rod is divided into ① and ② parts; the telescopic rod is divided into ③ and ④ parts, and ② in the swing rod coincides with ③ in the telescopic rod. As there were degrees of freedom in the mechanism, the stiffness matrix was singular. The B_iC_i of the moving pair could be regarded as a rigid connection to eliminate the rigid degrees of freedom; hence, the moving mechanism could be regarded as an "instantaneous structure" in a short period of time. A_i was a Hooke joint connecting the UPS and the fixed platform. As the Hooke hinge connection can be regarded as a composite of two rotation pairs whose axes are perpendicular to one another, the curvature of the two equivalent rotation pairs at the A_i node was zero. A_i was connected to a fixed platform; therefore, the elastic displacement at point A_i and the elastic rotation angle in the two rotation directions were also zero. In other words, there were only two generalized coordinates for the elastic rotation angle and curvature around the Z_{Ai}-axis at point A_i. The coupling technology of finite element node degrees of freedom was used to model the relationship between the telescopic rod and the swing rod. Point B_i on the swing rod and B_i on the telescopic rod were 3-DOF couplings, and their elastic displacements were the same. There was a 6-DOF coupling between C_i on the swing rod and C_i on the telescopic rod, and its elastic displacement and elastic rotation angle were the same. There was a fixed connection between D_i on the swing rod and D_i on the composite ball hinge, and there was a DOF around the Z_{Ai} direction, so its elastic displacement and elastic rotation angle were the same. And the rotation angle and curvature in the Z_{Ai} direction were zero. Point a_i was a composite spherical hinge, and only the rotation angle and curvature around the Z_{Ai}-axis were non-zero elastic deformations: the rest were zero. As shown in Figure 6, the deformation of the branched chain can be represented by u_{i1}–u_{i48}.

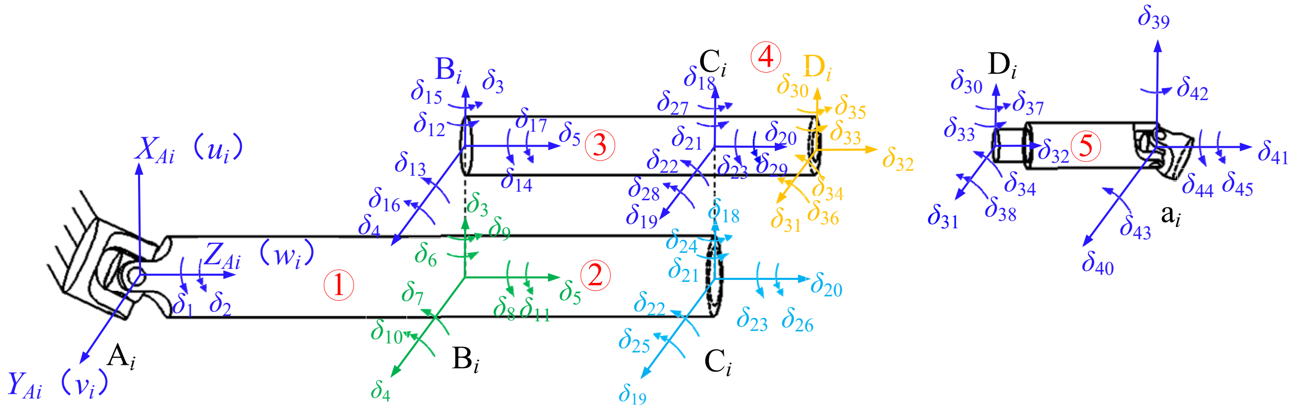

Figure 5. Generalized coordinates of UPS branch chain in the element coordinate system.

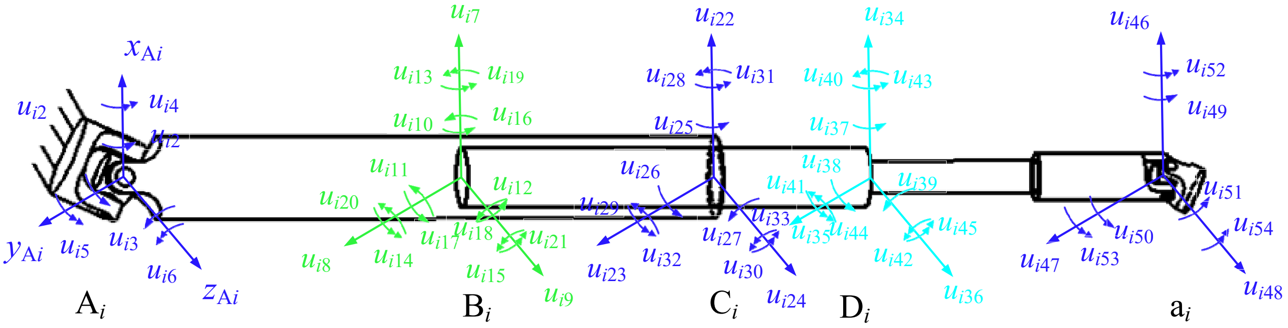

Figure 6. Generalized coordinates of UPS branch chain in reference coordinate system.

The element coordinate system A_i-$x_{Ai}y_{Ai}z_{Ai}$ was established at A_i of the A_iB_i element, and the posture of the coordinate system was the same as that of the fixed coordinate system A_i-$u_iv_iw_i$ (i = 1, 2, 3) of the UPS branch chain. Similarly, the element coordinate system was also established at nodes B_i, C_i, D_i, and a_i. Then, the posture transformation matrix from the element coordinate system A_i-$x_{\mathrm{A}i}y_{\mathrm{A}i}z_{\mathrm{A}i}$ to the reference coordinate system O_1-$x_1y_1z_1$ could be expressed as

$$R_{i1} = \begin{bmatrix} c\phi_i & 0 & -s\phi_i \\ s\varphi_i s\phi & c\varphi_i & s\varphi_i c\phi_i \\ c\varphi_i s\phi_i & -s\varphi_i & c\varphi_i c\phi \end{bmatrix} \tag{8}$$

As the attitude transformation matrix was an orthogonal matrix, the attitude transformation matrices from the reference coordinates O_1-$x_1y_1z_1$ to the A_i, B_i, C_i, and D_i coordinate systems were as follows:

$$R_{ik} = {R_{ik}}^{-1} = {R_{ik}}^{T} = \begin{bmatrix} c\phi_{ik} & s\varphi_{ik}s\phi_{ik} & c\varphi_{ik}s\phi_{ik} \\ 0 & c\varphi_{ik} & -s\varphi_{ik} \\ -s\phi_{ik} & s\varphi_{ik}c\phi_{ik} & c\varphi_{ik}c\phi_{ik} \end{bmatrix} (i = 1,2,3; k = 1,2,3,4,5) \tag{9}$$

Then, the transformation relationship between the element generalized coordinate system and the system generalized coordinate system of element components ①, ②, ③, ④, and ⑤ is as follows:

$$\begin{aligned}
\delta_{\mathrm{A}i\mathrm{B}i} &= diag\big(\boldsymbol{R}_{i1} \quad \boldsymbol{R}_{i1} \quad \boldsymbol{R}_{i1} \quad \boldsymbol{R}_{i1} \quad \boldsymbol{R}_{i1} \quad \boldsymbol{R}_{i1}\big)\boldsymbol{u}_{\mathrm{A}i\mathrm{B}i} \\
\delta_{2\mathrm{B}i\mathrm{C}i} &= diag\big(\boldsymbol{R}_{i2} \quad \boldsymbol{R}_{i2} \quad \boldsymbol{R}_{i2} \quad \boldsymbol{R}_{i2} \quad \boldsymbol{R}_{i2} \quad \boldsymbol{R}_{i2}\big)\boldsymbol{u}_{2\mathrm{B}i\mathrm{C}i} \\
\delta_{3\mathrm{B}i\mathrm{C}i} &= diag\big(\boldsymbol{R}_{i2} \quad \boldsymbol{R}_{i2} \quad \boldsymbol{R}_{i2} \quad \boldsymbol{R}_{i2} \quad \boldsymbol{R}_{i2} \quad \boldsymbol{R}_{i2}\big)\boldsymbol{u}_{3\mathrm{B}i\mathrm{C}i} \\
\delta_{\mathrm{C}i\mathrm{D}i} &= diag\big(\boldsymbol{R}_{i3} \quad \boldsymbol{R}_{i3} \quad \boldsymbol{R}_{i3} \quad \boldsymbol{R}_{i3} \quad \boldsymbol{R}_{i3} \quad \boldsymbol{R}_{i3}\big)\boldsymbol{u}_{\mathrm{C}i\mathrm{D}i} \\
\delta_{\mathrm{D}i\mathrm{a}i} &= diag\big(\boldsymbol{R}_{i4} \quad \boldsymbol{R}_{i4} \quad \boldsymbol{R}_{i4} \quad \boldsymbol{R}_{i4} \quad \boldsymbol{R}_{i4} \quad \boldsymbol{R}_{i4}\big)\boldsymbol{u}_{\mathrm{D}i\mathrm{a}i}
\end{aligned}$$

where $\boldsymbol{\delta}$ is the element generalized coordinate and $\boldsymbol{u}$ is the system generalized coordinate.

The dynamic equation of elements ①, ②, ③, ④, and ⑤ is as follows:

$$\boldsymbol{M}_e^k \ddot{\boldsymbol{\delta}}^k + \boldsymbol{C}_e^k \dot{\boldsymbol{\delta}}^k + \boldsymbol{K}_e^k \boldsymbol{\delta}^k = \boldsymbol{F}_e^k + \boldsymbol{P}_e^k + \boldsymbol{Q}_e^k \tag{10}$$

where $\boldsymbol{M}_e^k$ is the mass matrix of the component, $\boldsymbol{C}_e^k$ is the damping matrix of the component, K_e^k is the stiffness matrix of the component, $\boldsymbol{\delta}^k$ is the generalized coordinates of the element at the k-th component, $\boldsymbol{F}_e^k$ is the external load, $\boldsymbol{P}_e^k$ is the force exerted by other components of the system, and $\boldsymbol{Q}_e^k$ is the inertia force of the rigid body.

The dynamic equation of the branched chain $\mathrm{A}_i\mathrm{a}_i$ in the system coordinates can be obtained by assembling the unit components ①, ②, ③, ④, and ⑤.

$$\boldsymbol{M}_e^i \ddot{u}_i + \boldsymbol{C}_e^i \dot{u}_i + \boldsymbol{K}_e^i u_i = \boldsymbol{F}_e^i + \boldsymbol{P}_e^i + \boldsymbol{Q}_e^i \tag{11}$$

where $\boldsymbol{M}_e^i$ is the mass matrix of branch chain i, $\boldsymbol{C}_e^i$ is the damping matrix of branch chain i, $\boldsymbol{K}_e^i$ is the stiffness matrix of branch chain i, u_i is the node system coordinate of branch chain i, $\boldsymbol{F}_e^i$ is the applied load of branch chain i, $\boldsymbol{P}_e^i$ is the force exerted on the branch chain i by other components of the system, and $\boldsymbol{Q}_e^i$ is the rigid body inertia force of branch chain i.

3.1.3. Elastic Dynamic Analysis of UP Branch Chain

The restrained branch UP was connected to a moving pair and static platform at the center point O_1 of the static platform through the hook hinge; thus, UP branch O_1O_2 could be regarded as a beam element. The generalized coordinates of O_1 were the same as those of A_i. Thus, UP branch O_1O_2 had 11 nonzero generalized coordinates. The generalized coordinates of UP restrained chain in element coordinate system and reference coordinate system are shown in Figures 7 and 8.

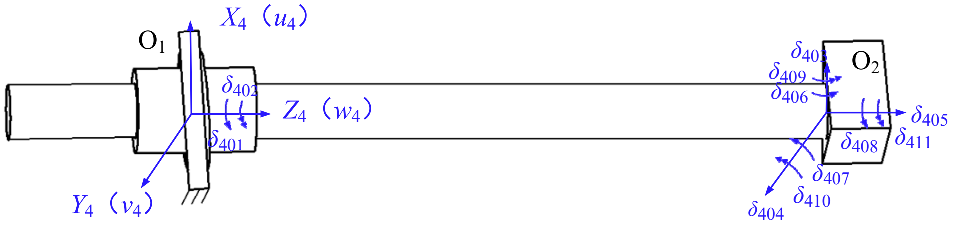

Figure 7. Generalized coordinates of UP restrained chain in element coordinate system.

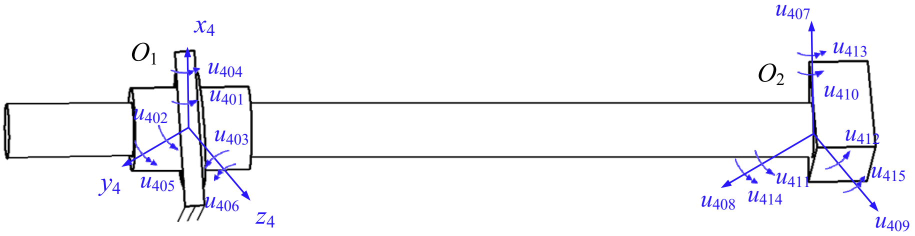

Figure 8. Generalized coordinates of UP restrained chain in reference coordinate system.

The element coordinate system O_1-$u_4v_4w_4$ was established at the O_1 point of the UP-constraint branch. Then, the posture transformation matrix from the element coordinate system to the reference coordinate system O_1-$x_4y_4z_4$ could be expressed as

$$\boldsymbol{R}_4 = \begin{bmatrix} c\phi_4 & s\varphi_4 s\phi_4 & c\varphi_4 s\phi_4 \\ 0 & c\varphi_4 & -s\varphi_4 \\ -s\phi_4 & s\varphi_4 c\phi_4 & c\varphi_4 c\phi \end{bmatrix} \tag{12}$$

The transformation relationship between the generalized coordinate system of the element and the generalized coordinate system of the UP branch chain is as follows:

$$\delta_{O1O2} = diag(\boldsymbol{R}_4 \quad \boldsymbol{R}_4 \quad \boldsymbol{R}_4 \quad \boldsymbol{R}_4 \quad \boldsymbol{R}_4 \quad \boldsymbol{R}_4)\boldsymbol{u}_{O1O2} \tag{13}$$

Then, the dynamic equation of the constrained branch chain in the system coordinates is given as:

$$\boldsymbol{M}_e^4 \ddot{u}_4 + \boldsymbol{C}_e^4 \dot{u}_4 + \boldsymbol{K}_e^4 u_4 = \boldsymbol{F}_e^4 + \boldsymbol{P}_e^4 + \boldsymbol{Q}_e^4 \tag{14}$$

where $\boldsymbol{M}_e^4$ is the mass matrix of the constrained branch chain, $\boldsymbol{C}_e^4$ is the damping matrix of the constrained branch chain, $\boldsymbol{K}_e^4$ is the stiffness matrix of the constrained branch chain, u_4 is the node system coordinate of the constrained branch chain, $\boldsymbol{F}_e^4$ is the applied load of the constrained branch chain, $\boldsymbol{P}_e^4$ is the force exerted on the constrained branch chain by other components of the system, and $\boldsymbol{Q}_e^4$ is the rigid body inertia force of the constrained branch chain.

3.1.4. Constraints for the 5-DOF-HPR

The stiffness of the moving platform was much greater than that of the branch chain component. Therefore, the elastic deformation of the moving platform could be ignored. The rigid body in space had six independent DOFs, so the displacement of the moving platform and each branch chain connection node was not independent. It was a function of six independent parameters of the moving platform and satisfied the following conditions. (1) Kinematic constraints: the displacement of the connection point between the branch chain and moving platform must be consistent with the displacement of the connection point between the moving platform and branch chain; (2) Dynamic constraints: the sum of the forces of each branch chain on the moving platform should be balanced with the external force and inertial force acting on the moving platform. The constraint relationship between the moving platform and the branch chain is shown in Figure 9.

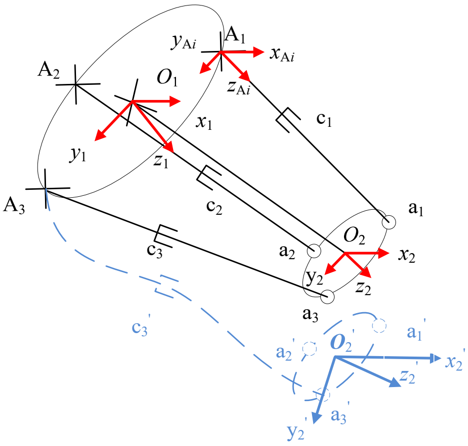

Figure 9. Constraint relationship between moving platform and branch chain (The light blue part of the figure is the displacement caused by elastic deformation of the component).

Suppose the transformation rotation matrix of the dynamic coordinate system O_2-$x_2y_2z_2$ relative to the fixed coordinate system O_1-$x_1y_1z_1$ is ${}^{O_1}_{O_2}R$. Assuming that the actual posture of the moving platform is at O_2, the actual posture of the moving platform changes slightly ($\delta\alpha$, $\delta\beta$, $\delta\gamma$, δx_2, δy_2, and δz_2) owing to the elastic deformation of the system branch chain, making the O_2 point move to $O_2{}'$; the transformation matrix from coordinate system O_2-$x_2y_2z_2$ to coordinate system $O_2{}'$-$x_2{}'y_2{}'z_2{}'$ is ΔR.

$$\Delta R = \begin{bmatrix} c(\delta\alpha)c(\delta\beta) & c(\delta\alpha)s(\delta\beta)s(\delta\gamma) - s(\delta\alpha)c(\delta\gamma) & c(\delta\alpha)s(\delta\beta)c(\delta\gamma) + s(\delta\alpha)s(\delta\gamma) & \delta x_{O_2} \\ s(\delta\alpha)c(\delta\beta) & s(\delta\alpha)s(\delta\beta)s(\delta\gamma) + c(\delta\alpha)c(\delta\gamma) & s(\delta\alpha)s(\delta\beta)c(\delta\gamma) - c(\delta\alpha)s(\delta\gamma) & \delta y_{O_2} \\ -s(\delta\beta) & c(\delta\beta)s(\delta\gamma) & c(\delta\beta)c(\delta\gamma) & \delta z_{O_2} \\ 0 & 0 & 0 & 1 \end{bmatrix} \tag{15}$$

Given the minimal deformation of the parallel module, the alternations in the orientation and position parameters of the moving platform resulting from the elastic deformation of the branch chain approached negligibility. Applying Taylor's formula and McLaughlin's expansion, it can be concluded that:

$$\begin{cases} c(\delta\alpha) \approx 1 \\ s(\delta\alpha) \approx \delta\alpha \end{cases} \quad \begin{cases} c(\delta\beta) \approx 1 \\ s(\delta\beta) \approx \delta\beta \end{cases} \quad \begin{cases} c(\delta\gamma) \approx 1 \\ s(\delta\gamma) \approx \delta\gamma \end{cases}$$

The coordinate transformation matrix can be rewritten as:

$$\Delta R \approx \begin{bmatrix} 1 & -\delta\alpha & \delta\beta & \delta x_{O_2} \\ \delta\alpha & 1 & \delta\gamma & \delta y_{O_2} \\ -\delta\beta & \delta\gamma & 1 & \delta z_{O_2} \\ 0 & 0 & 0 & 1 \end{bmatrix} \tag{16}$$

Therefore, the coordinate transformation matrix from the coordinate system $O_2{}'$-$x_2{}'y_2{}'z_2{}'$ after elastic deformation to the reference coordinate system O_1-$x_1y_1z_1$ can be expressed as

$$ {}^{O_1}_{O_2{}'}R = \Delta R {}^{O_1}_{O_2}R \tag{17}$$

Then, the expression of the coordinate system $O_2{}'$-$x_2{}'y_2{}'z_2{}'$ in the reference coordinate system O_1-$x_1y_1z_1$ is

$$\begin{bmatrix} x'_{ai} \\ y'_{ai} \\ z'_{ai} \\ 1 \end{bmatrix}_{O_1} = \Delta R {}^{O_1}_{O'_2}R \begin{bmatrix} x_{ai} \\ y_{ai} \\ z_{ai} \\ 1 \end{bmatrix}_{O'_2} = \Delta R \begin{bmatrix} x_{ai} \\ y_{ai} \\ z_{ai} \\ 1 \end{bmatrix}_{O_1} \tag{18}$$

Further

$$\begin{bmatrix} \Delta x_{ai} \\ \Delta y_{ai} \\ \Delta z_{ai} \\ 0 \end{bmatrix}_{O_1} = \begin{bmatrix} x'_{ai} \\ y'_{ai} \\ z'_{ai} \\ 1 \end{bmatrix}_{O_1} - \begin{bmatrix} x_{ai} \\ y_{ai} \\ z_{ai} \\ 1 \end{bmatrix}_{O_1} = (\Delta R - E) \begin{bmatrix} x_{ai} \\ y_{ai} \\ z_{ai} \\ 1 \end{bmatrix}_{O_1} \tag{19}$$

where E denotes the identity matrix. In the fixed coordinate system O_1-$x_1y_1z_1$, the above equation can be expressed as:

$$\begin{bmatrix} \Delta x_{ai} \\ \Delta y_{ai} \\ \Delta z_{ai} \end{bmatrix} = \begin{bmatrix} 1 & & & & z_{ai} & -y_{ai} \\ & 1 & & -z_{ai} & & x_{ai} \\ & & 1 & y_{ai} & -x_{ai} & \end{bmatrix}_{O_1} \begin{bmatrix} \delta x_{O_2} \\ \delta y_{O_2} \\ \delta z_{O_2} \\ \delta \gamma \\ \delta \beta \\ \delta \alpha \end{bmatrix} \tag{20}$$

The equation of motion is abbreviated as:

$$\boldsymbol{q}_{ai} = \boldsymbol{J}_{ai} \boldsymbol{q}_0 \tag{21}$$

where $\boldsymbol{q}_{ai}$ is the elastic displacement of point a_i and $\boldsymbol{q}_0$ denotes the three displacements and three rotation variables of the moving platform. $\boldsymbol{J}_{ai}$ is a kinematic constraint matrix.

Considering the Z-Y-X Euler angles (α, β, γ) to represent the attitude of the moving platform $a_1a_2a_3$, the coordinate system O_2-$x_2y_2z_2$ fixed to the moving platform can be obtained from the fixed coordinate system O_1-$x_1y_1z_1$ by rotating angle α around the Z-axis, angle β around the Y-axis, and angle γ around the X-axis. Then, the posture transformation matrix from the system coordinate $\boldsymbol{U}_0$ to element coordinate δ_0 for the displacement change of movable platform $a_1a_2a_3$ caused by the elastic deformation of each branch chain component is as follows:

$$R_0 = \begin{bmatrix} c\alpha c\beta & s\alpha c\beta & -s\beta \\ c\alpha s\beta s\gamma - s\alpha c\gamma & s\alpha s\beta s\gamma + c\alpha c\gamma & c\beta s\gamma \\ c\alpha s\beta c\gamma + s\alpha s\gamma & s\alpha s\beta c\gamma - c\alpha s\gamma & c\beta c\gamma \end{bmatrix} \tag{22}$$

Then,

$$\delta_0 \;=\; \boldsymbol{B}_0 \, \boldsymbol{U}_0 \tag{23}$$

where $\boldsymbol{B}_0 = \begin{bmatrix} R_0 & \\ & R_0 \end{bmatrix}$, δ_0 = $[\delta_{01}\ \delta_{02}\ \delta_{03}\ \delta_{04}\ \delta_{05}\ \delta_{06}]^{\mathrm{T}}$, δ_0 is the displacement change of the movable platform caused by the elastic deformation of each branch chain component in the local coordinate system $O_2{'}$-$x_2{'}y_2{'}z_2{'}$, and $\boldsymbol{U}_0$ = $[u_1\ u_2\ u_3\ u_4\ u_5\ u_6]^{\mathrm{T}}$, where $\boldsymbol{U}_0$ is the displacement of the movable platform caused by the deformation of each branch chain component in the fixed coordinate system O_1-$x_1y_1z_1$.

The coupling effect between the nominal motion and the micro motion of the moving platform caused by the elastic deformation of the branched-chain components is not considered. From the foregoing analysis, in the reference coordinate system O_1-$x_1y_1z_1$, the speed and acceleration of the moving platform can be expressed as

$$\dot{u}_{O_1} = \begin{bmatrix} \dot{x}_{O_1} + \dot{u}_1 \\ \dot{y}_{O_1} + \dot{u}_2 \\ \dot{z}_{O_1} + \dot{u}_3 \\ \dot{\gamma} + \dot{u}_4 \\ \dot{\beta} + \dot{u}_5 \\ \dot{\alpha} + \dot{u}_6 \end{bmatrix},\ \ddot{u}_{O_1} = \begin{bmatrix} \ddot{x}_{O_1} + \ddot{u}_1 \\ \ddot{y}_{O_1} + \ddot{u}_2 \\ \ddot{z}_{O_1} + \ddot{u}_3 \\ \ddot{\gamma} + \ddot{u}_4 \\ \ddot{\beta} + \ddot{u}_5 \\ \ddot{\alpha} + \ddot{u}_6 \end{bmatrix} \tag{24}$$

The dynamic equation of the moving platform of the system can be obtained as

$$\begin{bmatrix} m_0 & & & & & \\ & m_0 & & & & \\ & & m_0 & & & \\ & & & I_{xx} & I_{xy} & I_{xz} \\ & & & I_{yx} & I_{yy} & I_{yz} \\ & & & I_{zx} & I_{zy} & I_{zz} \end{bmatrix} \begin{bmatrix} \ddot{x}_{O_1} + \ddot{u}_1 \\ \ddot{y}_{O_1} + \ddot{u}_2 \\ \ddot{z}_{O_1} + \ddot{u}_3 \\ \ddot{\gamma} + \ddot{u}_4 \\ \ddot{\beta} + \ddot{u}_5 \\ \ddot{\alpha} + \ddot{u}_6 \end{bmatrix} = \begin{bmatrix} \sum F_{ix} \\ \sum F_{iy} \\ \sum F_{iz} \\ \sum M_{ix} \\ \sum M_{iy} \\ \sum M_{iz} \end{bmatrix} + \begin{bmatrix} \sum F_{O_1x} \\ \sum F_{O_1y} \\ \sum F_{O_1z} \\ \sum M_{O_1x} \\ \sum M_{O_1y} \\ \sum M_{O_1z} \end{bmatrix} \tag{25}$$

where $\sum F_{O1x}$, $\sum F_{O1y}$, and $\sum F_{O1z}$ are the components of the external force acting on the moving platform in th*e* X-, Y-, and Z-axis directions; $\sum M_{O1x}$, $\sum M_{O1y}$, and $\sum M_{O1z}$ are the components of the external torque acting on the moving platform around the X-, Y-, and Z-axes; $\sum F_{ix}$, $\sum F_{iy}$, and $\sum F_{iz}$ are the components of the resultant force of each branch chain acting on the moving platform in the X-, Y-, and Z-axis directions; $\sum M_{ix}$, $\sum M_{iy}$, and $\sum M_{iz}$ are the components of the torque of each branch chain acting on the moving platform around the X-, Y-, and Z-axes; $Ixx, \ldots, Izz$ are the moments of inertia and product of inertia of the moving platform; and m_0 is the mass of the moving platform.

This equation can be abbreviated (under dynamic constraint conditions) as:

$$\boldsymbol{M}_0\ddot{\boldsymbol{U}}_0 = \boldsymbol{f}_0 + \boldsymbol{F}_0 - \boldsymbol{M}_0\ddot{\boldsymbol{U}}_{0r} \tag{26}$$

where $\boldsymbol{M}_0$ is the generalized mass matrix of the moving platform, $\boldsymbol{f}_0$ is the resultant force matrix of the branched chain acting on the moving platform; $\boldsymbol{F}_0$ is the resultant force matrix of the external force acting on the moving platform, and $\ddot{\boldsymbol{U}}_{0r}$ is the nominal acceleration array of the moving platform.

3.1.5. System Dynamics Equation

Using the system dynamics constraint equations and combining the dynamic equations of each branch chain, the dynamic equation of the system can be expressed as

$$\boldsymbol{M}\ddot{\boldsymbol{U}} + \boldsymbol{C}\dot{\boldsymbol{U}} + \boldsymbol{K}\boldsymbol{U} = \boldsymbol{F} - \boldsymbol{M}\ddot{\boldsymbol{U}}_r \tag{27}$$

where $\boldsymbol{M}$ is the total mass matrix, $\boldsymbol{C}$ is the total damping matrix, $\boldsymbol{K}$ is the total stiffness matrix, $\boldsymbol{F}$ is the generalized force matrix, $\ddot{\boldsymbol{U}}_r$ is the rigid body acceleration matrix, $\boldsymbol{U}$ is the generalized coordinate array, and $\ddot{\boldsymbol{U}}$ is the elastic acceleration array.

The natural frequency of the 5-DOF-HPR was analyzed according to the established model. The natural frequency of the testing machine was related to its position and posture in the workspace. In the simulation, the parameters of the robot in the workspace were $\alpha = -30°$–$30°$, $\beta = -30°$–$30°$, $Z = 1400$ mm, $\alpha_1 = 0°$, and $\alpha_2 = 4°$. α, β, and Z were the pose parameters of the robot in its fixed coordinate system; α_1 was the angle of the first rotating head; and α_2 was the angle of the secondary rotating head.

According to the simulation results shown in Figure 10, the first four natural frequencies of the 5-DOF-HPR all presented a convex shape in the middle and a concave shape around the periphery, and the higher the order of the natural frequency, the larger the frequency span became. The first natural frequency ranged from 23 to 47 Hz; the second natural frequency ranged from 58 to 83 Hz; the third natural frequency ranged from 75 to 117 Hz; and the fourth natural frequency ranged from 110 to 158 Hz. As the first four natural frequencies varied from $\alpha = -30°$ to 30° and $\beta = -30°$ to 30°, the natural frequency exhibited a wide range of sudden changes, and the second- and third-order natural frequencies were the most obvious.

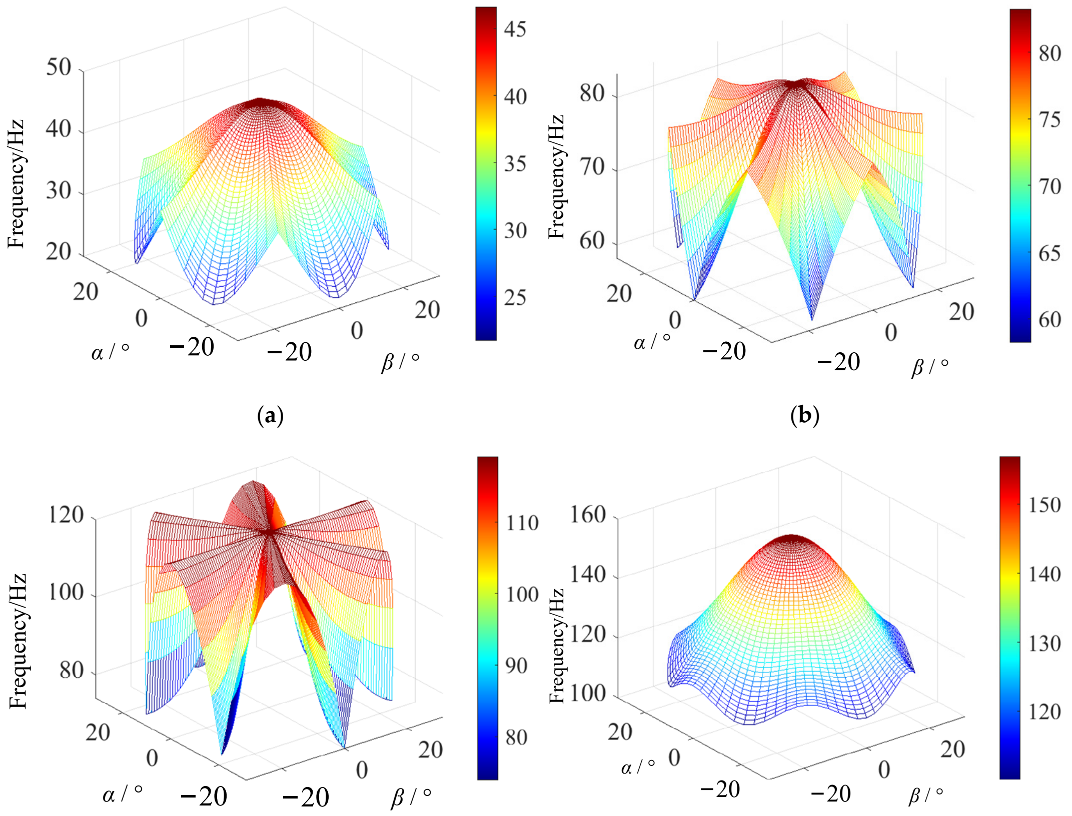

(**a**) (**b**)

(**c**) (**d**)

Figure 10. Initial four natural frequency models of the 5-DOF-HPR. (**a**) First-order natural frequency. (**b**) Second-order natural frequency. (**c**) Third-order natural frequency. (**d**) Fourth-order natural frequency.

3.2. Dynamic Characteristics Analysis of the FSS

The support cylinder must maintain a constant pressure during the working process, so it was assumed that the hydraulic oil in the FSS did not flow, allowing the fluid characteristics to be ignored during the analysis. The chamber filled with hydraulic oil was analyzed as a flexible component, so the entire cylinder could be simplified as a series of multiple springs and dampers.

The 36 support cylinders were simplified into 36 sets of springs and dampers, and the stiffness of each support cylinder was K^n ($n = 1, 2, \ldots, 36$).

As shown in Figure 11, M is the weight of the piston; F is the load applied by the optical mirror; ΔF is the local force applied by the polishing disc; K_1 is the stiffness of the beryllium bronze reed in the upper chamber; K_2 is the stiffness of the small diaphragm in the upper chamber; K_3 is the stiffness of the hydraulic oil in the upper chamber; K_4 is the stiffness of the large diaphragm; K_5 is the stiffness of the hydraulic oil in the lower chamber; K_6 is the stiffness of the small diaphragm in the lower chamber; and K_7 is the stiffness of the beryllium bronze reed in the lower chamber. C_1–C_7 denote the damping of each component.

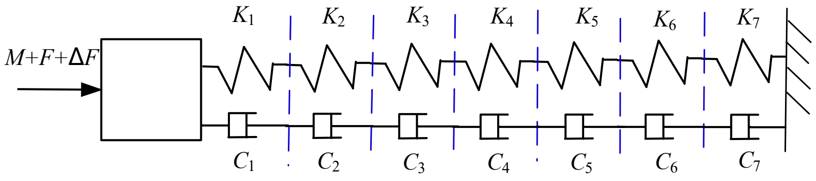

Figure 11. Spring model of support cylinder.

During the working process, the displacement of the support cylinder can be expressed as:

$$\Delta L = \frac{V_u - V_d}{2S} \tag{28}$$

where ΔL is the displacement of the support cylinder; ΔV_u is the volume change of the upper chamber; ΔV_d is the volume change of the lower chamber; and S is the cross-sectional area of the support piston.

When the support shaft of the support cylinder changes ΔL, the volume of the upper and lower chambers can be expressed as:

$$\boldsymbol{V}_u = f\left(\boldsymbol{W}, \boldsymbol{L}, \Delta L, \Delta L_1, \Delta L_3, \Delta L_4, \Delta L_6, R_p\right) \tag{29}$$

$$\boldsymbol{V}_d = f\left(\boldsymbol{W}, \boldsymbol{L}, \Delta L, \Delta L_2, \Delta L_3, \Delta L_5, \Delta L_6, R_p\right) \tag{30}$$

where $\boldsymbol{W} = \begin{bmatrix} W_1 & & \\ & \ddots & \\ & & W_m \end{bmatrix}$ and $\boldsymbol{L} = \begin{bmatrix} L_1 & & \\ & \ddots & \\ & & L_n \end{bmatrix}$ are the structural parameters of the support cylinder; m and n indicate the number of radial and axial structural parameters of the support cylinder; ΔL_1 is the extension quantity of the small rolling diaphragm in the upper chamber; ΔL_2 is the extension quantity of the small rolling diaphragm in the lower chamber; ΔL_3 is the extension quantity of the large rolling diaphragm; ΔL_4 is the compression quantity of the small rolling diaphragm in the upper chamber; ΔL_5 is the compression quantity of the small rolling diaphragm in the lower chamber; ΔL_6 is the compression quantity of the large rolling diaphragm; and R_p is the chamfer radius of the chamber.

Then, the hydraulic stiffnesses of the upper and lower chambers, respectively, are:

$$K_3 = \frac{\beta_e S^2}{V_u} \tag{31}$$

$$K_5 = \frac{\beta_e S^2}{V_d} \tag{32}$$

where β_e is the effective bulk modulus of elasticity of hydraulic oil.

According to the equation of the volume elastic coefficient, the effective volume elastic modulus of hydraulic oil can be expressed as:

$$\beta_e = -\frac{1}{\Delta p} \cdot \frac{\Delta V}{V} \tag{33}$$

The force required for the deformation of the beryllium bronze reed and rolling diaphragm in the positive and negative directions was analyzed using a finite element model to calculate the stiffnesses K_1, K_2, and K_4.

When operating in the autonomous constant-pressure support mode, the FSS exhibits stiffness curves for both large and small diaphragms at varying deformations (Figure 12). The red curve is the stiffness curve of the large rolling diaphragm, and the blue curve is the deformation curve of the small rolling diaphragm. It can be seen from the change in the curve that, although the rolling diaphragm is a nonlinear structure perpendicular to the deformation direction, its stiffness is approximately the same when the deformation in the positive and negative directions is the same.

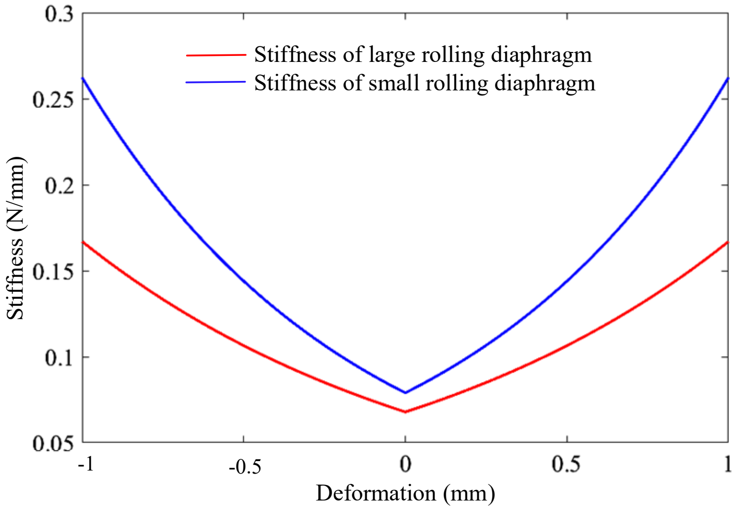

Figure 12. Stiffnesses of large and small rolling diaphragms.

The change in the stiffness of the beryllium–bronze spring from -1 mm to 1 mm deformation was analyzed using ANSYS 2022.R1, as shown in Figure 13. It can be seen from the curve that the stiffness of beryllium–bronze reed fluctuated within 0.6940–0.6965 N/mm, regardless of the movement in the positive or negative direction, and its fluctuation range was only 0.0025 N/mm. Within the allowable error range, the stiffness of beryllium bronze reed in the stroke range can be considered a constant value.

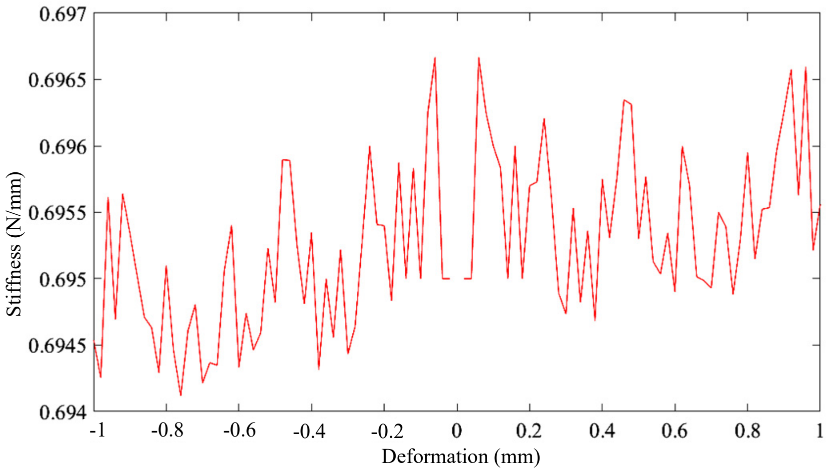

Figure 13. Stiffness of beryllium bronze reed.

Then, the natural frequency of the hydraulic system is:

$$\omega_0 = \sqrt{\boldsymbol{K}_0/\boldsymbol{m}_0} \tag{34}$$

where $\boldsymbol{K}_0$ is the stiffness matrix of the support cylinder and $\boldsymbol{m}_0$ is the mass matrix of the support cylinder.

According to the established model, the natural frequency of the support cylinder was analyzed. The first four natural frequencies of the support cylinder at different support heights and working pressures are shown in Figure 14. The first-order natural frequency ranged from 8.0 to 8.3 Hz; the second-order natural frequency ranged from 12 to 16.5 Hz; the third-order natural frequency ranged from 16 to 25.5 Hz; and the fourth-order natural frequency ranged from 25.5 to 35 Hz. The changing trends of the first four natural frequencies are symmetrical structures in the positive and negative directions of motion. Therefore, in the follow-up research work, it is only necessary to analyze the motion of the FSS in one direction. The first and second frequencies changed relatively smoothly. The third and fourth natural frequencies had a greater curvature in the direction of the support height displacement. When the support pressure was changed, the natural frequency changes were not obvious.

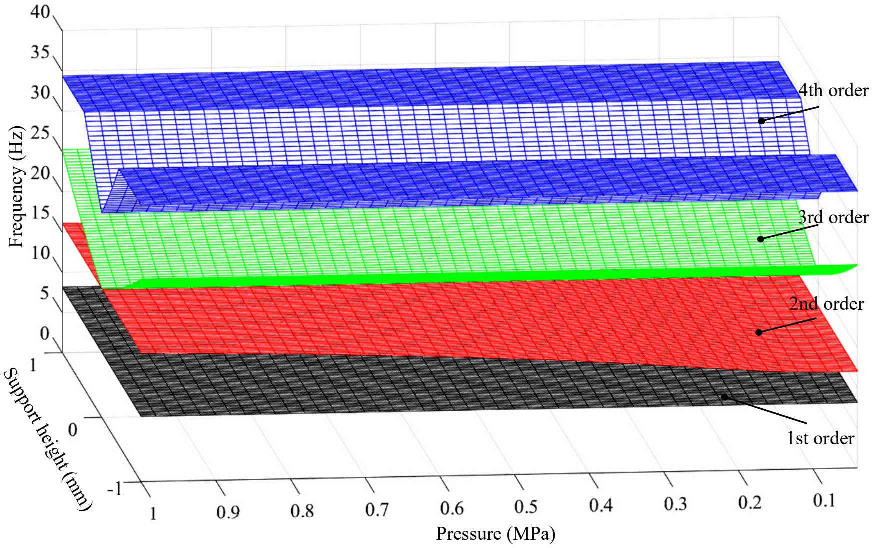

Figure 14. Natural frequency of support cylinder.

3.3. Dynamic Characteristics Analysis of the CCOS Grinding System

As the revolution motor rotates, the planetary polishing tool system generates force and torque on the 5-DOF-HPR. The force analysis of the CCOS grinding system is shown in Figure 15.

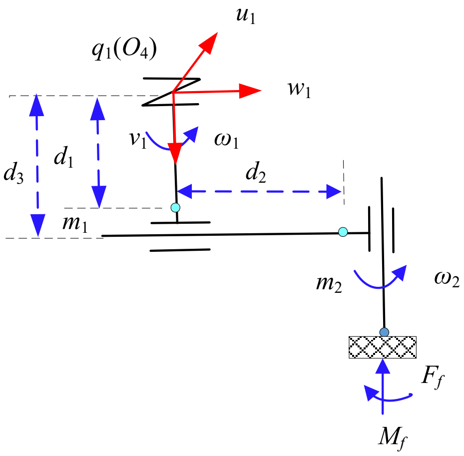

Figure 15. Force analysis of CCOS grinding system.

In the revolution module, the speed of the revolution motor is ω_1; the total mass of the module is m_1; and the mass center is located on the axis of the revolution motor. The mass center coordinate m_1 is ${}^{O_4}m_1 = (0, d_1, 0)$ in the coordinate system O_4-$u_1v_1w_1$. In the rotation module, the total mass of the module is m_2; the center of mass is located on the eccentric rod; its distance from the axis of the revolution motor is d_2, and the center of mass coordinate m_2 is ${}^{O_4}m_2 = [\cos(\omega_1 t)d_2, d_3, -\sin(\omega_1 t)d_2]$ in the coordinate system O_4-$u_1v_1w_1$. When the revolution motor rotates, it produces a centrifugal force F_{ml}. At the same time, the tool system bears the reaction force F_{if} from the mirror and its own gravity. The equations of centrifugal force, reaction force, and gravity are as follows:

$$\begin{cases} F_{ml} = m_2\omega_1 d_2 \\ F_{if} = P_m S_m \\ G_C = (m_1 + m_2)g \end{cases} \tag{35}$$

where S_m is the contact area between the grinding disc and the mirror and P_m is the cylinder pressure.

During processing, assuming that the angle between the eccentric rod and the original position is $\omega_1 t$ and the direction of the force is in the coordinate system O_4-$u_1v_1w_1$, the centrifugal force F_{ml} and the reaction force F_{if} are expressed as:

$$\begin{cases} {}^{O_4}F_{ml} = F_{ml}e_{ml} = [F_{ml}\cos(\omega_1 t), 0, -F_{ml}\sin(\omega_1 t)d_2]^{\mathrm{T}} \\ {}^{O_4}F_{if} = F_{if}e_{if} = \left[0, F_{if}, 0\right]^{\mathrm{T}} \end{cases} \tag{36}$$

where e_{ml} is the direction vector of the centrifugal force and e_{if} is the direction vector of the reaction force.

4. Dynamic Characteristic Measurement Experiment

4.1. Natural Frequency Measurement Experiment of the LOMPS

In the context of optical mirror processing, robotic systems may experience resonance due to natural frequencies at various orientations, resulting in additional forces being exerted on the end effector during grinding operations. These unintended forces can significantly impact the quality of large-scale optical mirror processing systems. Consequently, it is imperative to conduct comprehensive dynamic characteristic analyses to establish a solid foundation for subsequent trajectory planning and optimization. The modal test was carried out by pulse excitation, and the hammering mode was used as the excitation input. An LC-2 force hammer (Donghua Test, Taizhou, China) was used as the exciting hammer, and its sensor was a YDL-4X piezoelectric quartz force sensor (Donghua Test, China). The collected force signal was transformed, processed, and amplified through a DHF-7 charge amplifier (Donghua Test, China), and the signal was transmitted to the tester. The acceleration sensors were a 608A11 ICP single-axis acceleration (Donghua Test, China) sensor and 605B31 ICP three-axis acceleration (Donghua Test, China) sensor from the PCB Company. The DH5923N tester (Donghua Test, China) and DHDAS analysis software (DHDAS V1.3) were used for the test and analysis system. The collected signal was recorded and processed by a tester, and it was further processed, converted, and calculated using analytical software. The natural frequency, vibration mode, and other modal parameters of the testing machine system were obtained. The experimental prototype is illustrated in Figure 16.

Figure 16. Experimental prototype.

4.1.1. Modal Experiment of the 5-DOF-HPR

During the experiment, the excitation point was located at the end of the secondary rotating head, and the vibration pickup points were arranged at the secondary rotating head, first rotating head, moving platform, compound spherical hinge, telescopic rod, telescopic sleeve, Hooke hinge, and drive motor. Each measuring point measured the acceleration response in the X, Y, and Z directions. The layout of the measuring points of the experimental prototype is shown in Figure 17. To avoid the randomness of the collected data, five hammering experiments were carried out at each vibration measuring point. The modal information of four different postures was collected, and the average value was taken as the final experimental result.

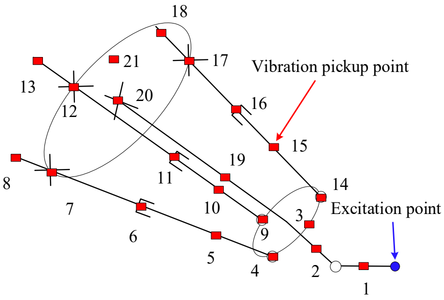

Figure 17. Distribution of vibration measuring points.

DHDAS software was used to calculate and analyze the measured data. The first four natural frequencies of the testing machine in four typical postures were measured. Posture 1: $\alpha = 0°$, $\beta = -15°$, $Z = 1200$ mm, $\alpha_1 = 0°$, $\alpha_2 = 12°$; Posture 2: $\alpha = 35°$, $\beta = 0°$, $Z = 1400$ mm, $\alpha_1 = -4°$, $\alpha_2 = -9°$; Posture 3: $\alpha = 0°$, $\beta = 20°$, $Z = 1250$ mm, $\alpha_1 = 0°$, $\alpha_2 = 24°$; and Posture 4: $\alpha = 0°$, $\beta = 0°$, $Z = 1600$ mm, $\alpha_1 = 0°$, $\alpha_2 = 0°$. The experimental results are shown in Figure 18.

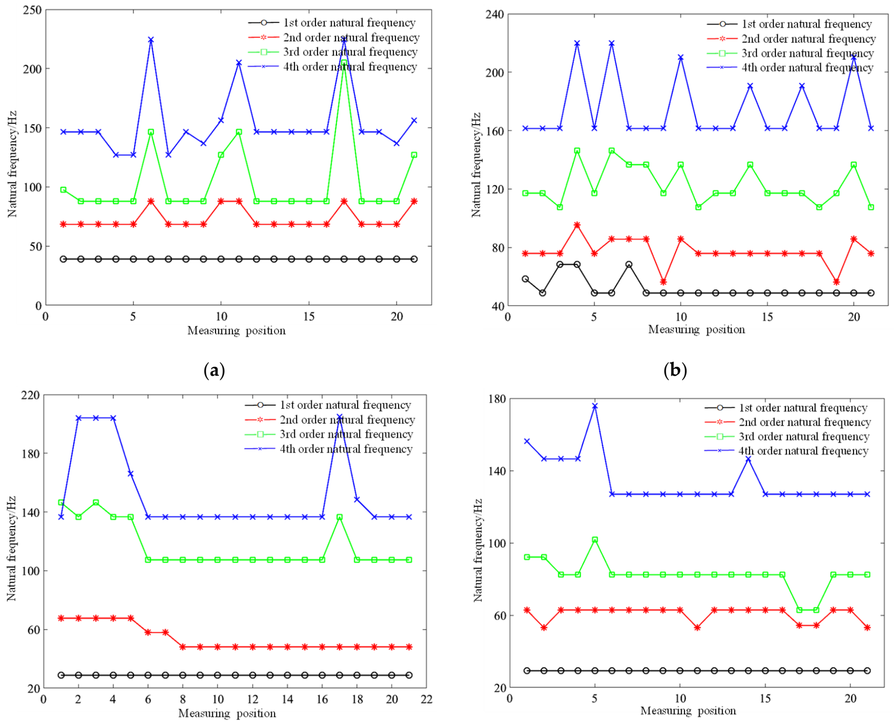

(**a**) (**b**)

(**c**) (**d**)

Figure 18. First four natural frequencies of 5-DOF-HPR. (**a**) Natural frequency of posture 1. (**b**) Natural frequency of posture 2. (**c**) Natural frequency of posture 3. (**d**) Natural frequency of posture 4.

As shown in Figure 18, although the collected experimental data of the first four natural frequencies of the four different postures fluctuated, they were all stable at a certain value. Through the analysis, it can be concluded that this was because the selected time was different when fast Fourier transform was performed using DHDAS, resulting in inconsistent natural frequencies or loss of certain natural frequencies. Therefore, the frequency that appeared more frequently was regarded as the natural frequency value of this order. A comparison between the first four natural frequencies and the simulation values of the 5-DOF-HPR is shown in Table 1.

Table 1. Natural frequencies of typical poses of the 5-DOF-HPR.

Natural Frequency		1st Order	2nd Order	3rd Order	4th Order
Posture 1	Simulation calculation value (Hz)	34.453	59.199	79.452	127.587
	Experimental test value (Hz)	39.063	68.359	87.891	146.484
	Relative error	11.8%	13.4%	9.6%	12.9%
Posture 2	Simulation calculation value (Hz)	44.238	70.554	103.594	147.908
	Experimental test value (Hz)	48.828	78.568	117.188	161.826
	Relative error	9.4%	10.2%	11.6%	8.6%
Posture 3	Simulation calculation value (Hz)	35.085	60.079	80.301	133.242
	Experimental test value (Hz)	38.726	67.656	89.422	147.719
	Relative error	9.4%	11.2%	10.2%	9.8%
Posture 4	Simulation calculation value (Hz)	25.957	56.876	74.212	111.084
	Experimental test value (Hz)	29.297	62.846	82.642	126.953
	Relative error	11.4%	9.5%	10.2%	12.5%

The data presented in Table 1 demonstrate that the error of the first four natural frequencies measured by the experiments were within 13.4%. These errors were due to the simplifying assumptions when establishing the elastodynamic model, and there were some errors between the actual pose of the robot and the model parameters. In summary, the error was within an acceptable range, and the natural frequency of the system calculated by the simulation reflected the actual natural frequency of the testing machine system to a certain extent, which verified the accuracy of the elastodynamic model of the 5-DOF-HPR. Further analysis of the first four natural frequencies of the 5-DOF-HPR at four different positions showed that, when the 5-DOF-HPR was in different positions, there was a large difference between the natural frequencies, especially when the range ratio of the first natural frequency reached 151%. The resonance phenomenon in the workspace should be avoided when path planning and parameter setting of the 5-DOF hybrid robot are carried out.

4.1.2. Modal Experiment of the FSS

The locations of the excitation point and vibration measurement points of the modal experiment of the FSS are shown in Figure 19. The excitation point was selected as the center of the support base plate, and the vibration measurement points were the support cylinders.

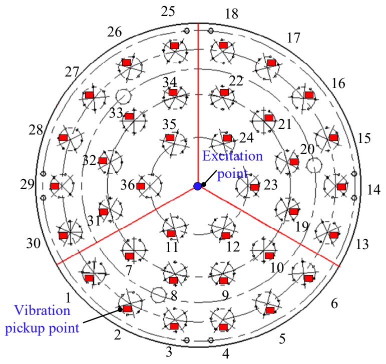

Figure 19. Vibration measurement points and excitation point location of the FSS.

According to the simulation results summarized in Section 3.2, the natural frequency of the support cylinder was mainly affected by the support height, and the change in the support pressure did not affect it. Therefore, during the experiment, the support pressure of the FSS was maintained at 0.5 MPa, and the support height was varied. The experimental process was the same as that described in Section 4.1.1. Each vibration measurement point was subjected to five hammering experiments. The modal information of four different postures was collected, and the average value was taken as the final experimental result. The experimental results are presented in Figure 20. The analysis method was the same as that in Section 4.1.1, and the comparison between the first four natural frequencies and simulation values of the FSS is shown in Table 2.

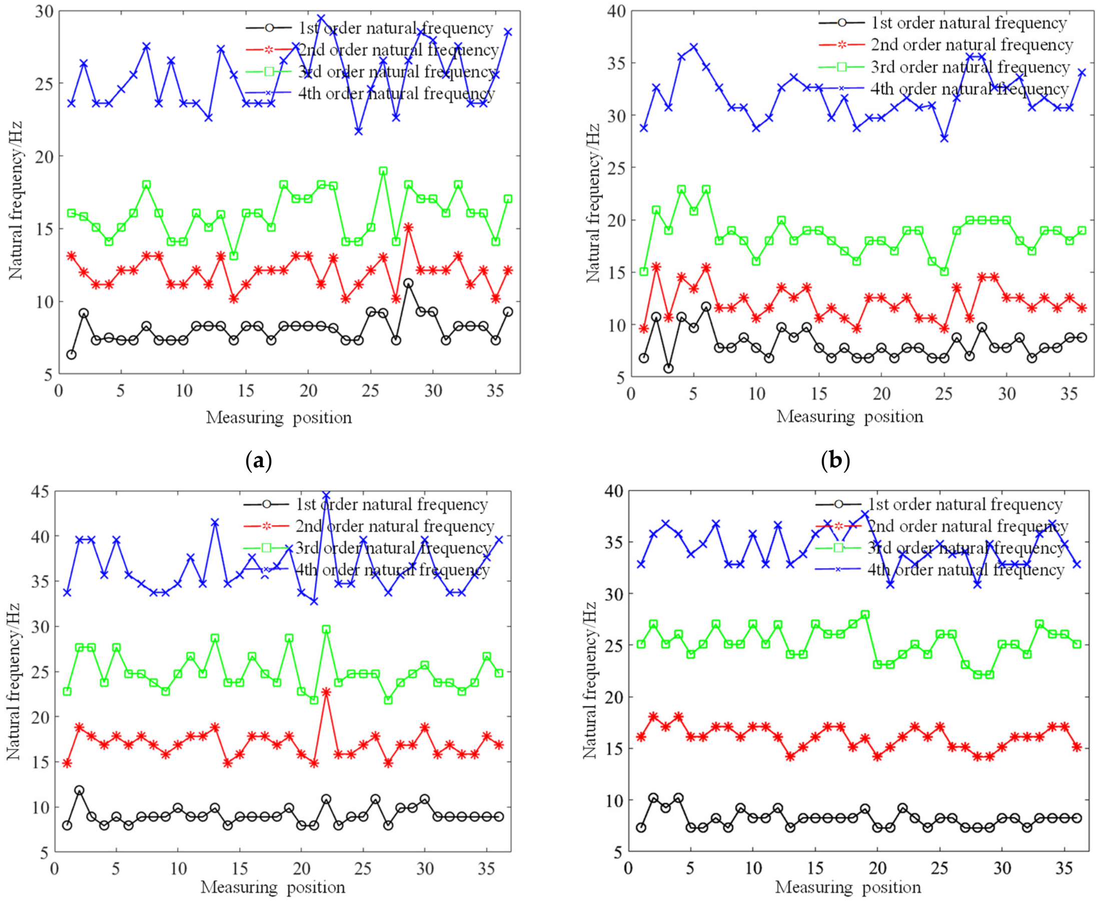

(**a**) (**b**)

(**c**) (**d**)

Figure 20. First four natural frequencies of FSS. (**a**) Displacement of the FSS of 0 mm. (**b**) Displacement of the FSS of 0.35 mm. (**c**) Displacement of the FSS of 0.70 mm. (**d**) Displacement of the FSS of 1.00 mm.

Table 2. Natural frequencies of typical postures of FSS.

Natural Frequency		1st Order	2nd Order	3rd Order	4th Order
Posture 1	Simulation calculation value (Hz)	8.136	12.065	16.09	25.434
	Experimental test value (Hz)	8.970	13.773	18.181	29.747
	Relative error	9.3%	12.4%	11.5%	14.5%
Posture 2	Simulation calculation value (Hz)	8.124	12.104	18.582	31.771
	Experimental test value (Hz)	9.274	13.993	21.139	36.062
	Relative error	12.4%	13.5%	12.1%	11.9%

Table 2. *Cont.*

Natural Frequency		1st Order	2nd Order	3rd Order	4th Order
Posture 3	Simulation calculation value (Hz)	8.180	14.845	23.251	34.390
	Experimental test value (Hz)	9.069	16.999	24.902	36.428
	Relative error	9.8%	12.67%	7.9%	5.6%
Posture 4	Simulation calculation value (Hz)	8.187	16.124	25.234	34.395
	Experimental test value (Hz)	9.476	18.490	29.934	38.997
	Relative error	13.6%	12.8%	15.7%	11.8%

It can be seen from Table 2 that the errors of the first four natural frequencies measured by the experiments were within 16% compared with the simulation data. This was due to the simplification of some parts in the vibration differential equation modeling of the FSS. In addition, the beryllium bronze reed and rolling diaphragms were non-linear elastic deformation components. When analyzing them, the finite-element method was used to analyze their stiffness, and there were some errors. In addition, the working pressure of the FSS was relatively low and was easily affected by environmental temperature, vibration, and other factors, potentially contributing significantly to the error. In summary, the error was within an acceptable range. The natural frequency calculated by simulation reflected the actual natural frequency of the FSS to a certain extent, which verified the accuracy of the elastodynamic model of the FSS.

Further analysis of the first four natural frequencies of the FSS in four different positions showed that, when the support displacement of the FSS increased, all the natural frequencies increased, except for the first natural frequency, which was basically unchanged. This was caused by the nonlinear elastic deformation of the beryllium bronze spring and the rolling diaphragm. The greater the deformation was, the greater the stiffness that was overcome, and the natural frequency also increased. During the working process of the FSS, the support height should be appropriately increased in the positive direction or decreased in the negative direction, when the support conditions permit, to increase the natural frequency of the FSS.

4.1.3. Modal Experiment of the FSS and "Mirror"

In the experiment, an aluminum plate was installed on the FSS instead of a mirror. The positions of the excitation point and the vibration measurement points on the aluminum plate coincided with the vertical projection of the excitation point and the vibration measurement points of the bottom support in Figure 19. Similarly, five hammering experiments were carried out at each vibration measuring point. The modal information at four different positions was collected, and the average value was taken as the final experimental result. The experimental results are presented in Figure 21.

As shown in Table 3, it can be seen that the first four natural frequencies increased compared with the FSS alone. This was because the installation of the mirror constrained each support point of the FSS, resulting in a constraint relationship between the vibration of each support cylinder. In addition, the natural frequency of the FSS and "mirror" was related to the quality, density, and size of the mirror. Therefore, in the process of optical mirror processing, to understand the natural frequency of the FSS and "mirror", it is necessary to analyze the system according to the specific mirror surface to be processed to ensure the accuracy of the processing system.

Table 3. Natural frequencies of typical postures of FSS and "mirror".

Natural Frequency		1st Order	2nd Order	3rd Order	4th Order
Posture 1	Experimental test value (Hz)	9.471	17.646	26.929	36.617
Posture 2		10.317	18.355	29.502	42.909
Posture 3		10.686	23.806	31.947	47.457
Posture 4		10.3878	24.620	36.3855	51.538

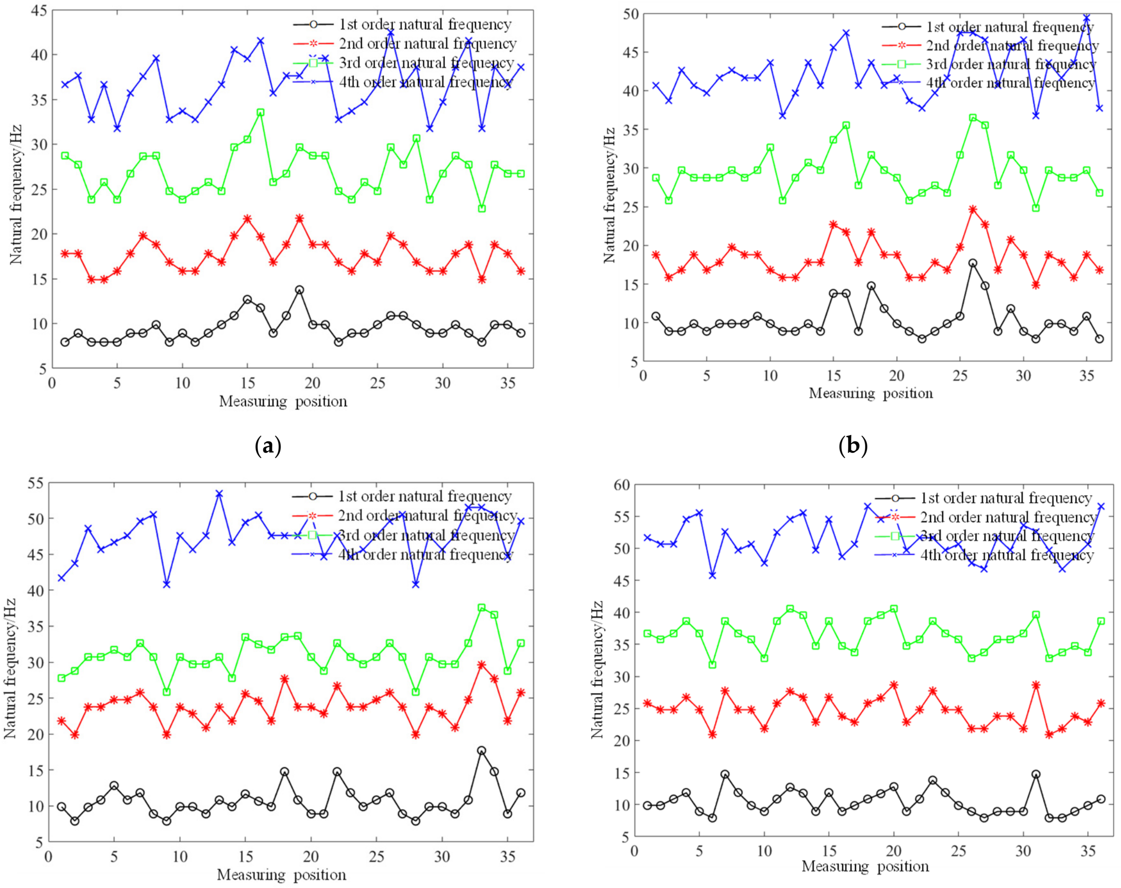

(**a**) (**b**)

(**c**) (**d**)

Figure 21. First four natural frequencies of FSS and "mirror". (**a**) Displacement of the FSS of 0 mm. (**b**) Displacement of the FSS of 0.35 mm. (**c**) Displacement of the FSS of 0.70 mm. (**d**) Displacement of the FSS of 1.00 mm.

4.2. Amplitude Experiment

The validity and accuracy of the mathematical model were further verified by collecting the vibration state of the mirror of the LOMPS under different working conditions. During the experiment, a 3-DOF acceleration sensor was installed on the mirror, and the vibration information of the mirror in the *X*-, *Y*-, and *Z*-directions was collected.

4.2.1. Amplitude of the 5-DOF-HPR at Different Running Speeds

During optical mirror processing, the dwell time at each point was determined by the running speed of the 5-DOF-HPR. The length of the robot's dwell time directly impacted the amount of mirror removal. To determine the optimal running speed of 5-DOF-HPR, avoid the resonance of the LOMPS, and improve the accuracy of the mirror to be processed, it is necessary to carry out further experimental acquisition of the amplitude of the mirror at different speeds. Through the control, the support height of the FSS was maintained at 0.8 mm, a grinding force of 20 N was applied to the CCOS grinding system, and the rotation speed was 30 Hz. The optical mirror machining robot was made to walk in a circle with a diameter of 400 mm on the mirror, and the amplitude of the mirror to be machined was measured by changing the running time of the 5-DOF-HPR. In the world coordinate system, the trajectory curve is as follows:

$$\begin{cases} X = 200\cos(2\pi t) \\ Y = 200\sin(2\pi t) \\ Z = 0 \end{cases} \tag{37}$$

The vibration information collected by the 5-DOF-HPR walking through the trajectory given by Equation (33) at 40–180 s is shown in Figure 22. When the running time changed, although the collected vibration amplitude fluctuated and the robot moved faster, the amplitude of the machined mirror in the *X*-, *Y*-, and *Z*-directions increased. During the working process, the operating speed of the 5-DOF-HPR should be reduced as much as possible on the premise of satisfying the processing technology and residence time requirements.

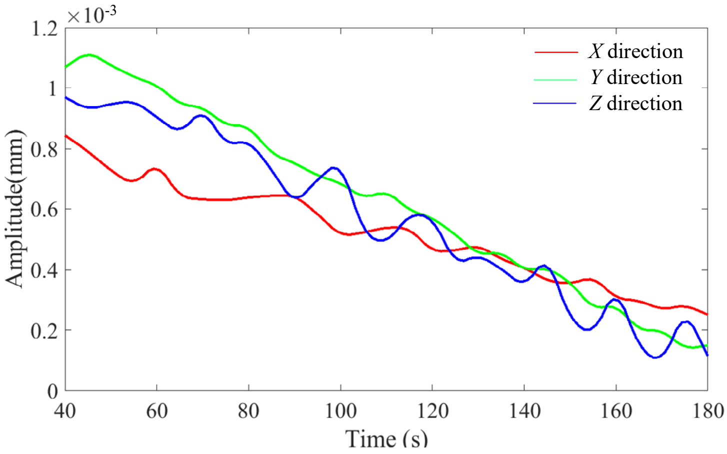

Figure 22. Amplitude of the 5-DOF-HPR at different speeds.

4.2.2. Amplitude Under Different Support Heights

In the experimental process with different support heights, the 5-DOF-HPR completed the circular trajectory in 140 s, and the speed of the CCOS grinding system was 30 Hz. The amplitudes of different support heights were measured by changing the support height of the FSS. The experimental results are presented in Figure 23.

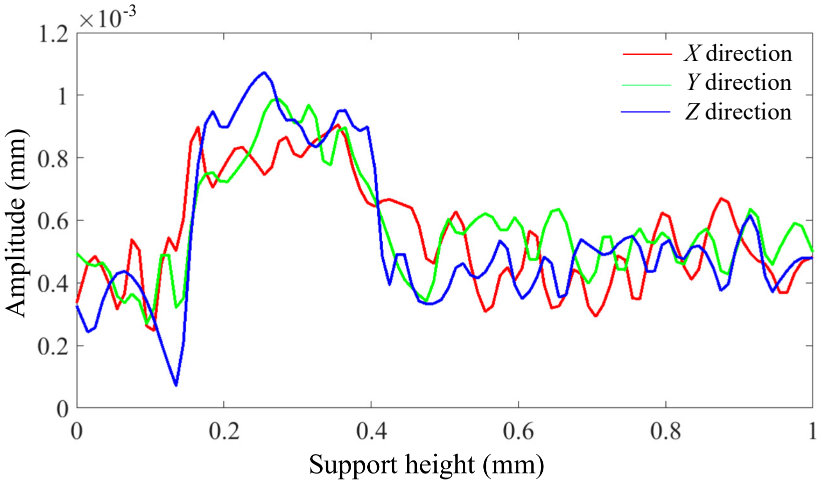

Figure 23. Amplitude of the FSS under different support heights.

According to the experimental results collected in Figure 23, when the support height of the FSS was 0.3 mm, the amplitude of the machined mirror increased significantly. This was because the rotation speed of the CCOS grinding system was set to 30 Hz, and the FSS exhibited a resonance phenomenon, which further verified the accuracy and validity of the established mathematical model. In the working process of the LOMPS, on the premise of meeting the requirements of the processing technology and support height, the revolution frequency of the CCOS grinding system should avoid the natural frequency of FSS and "mirror", so as to avoid resonance and reduce the processing accuracy of the optical mirror.

4.2.3. Amplitude of the CCOS Grinding System at Different Speeds

During the experiment, the 5-DOF-HPR completed a circular trajectory in 140 s. The support height of the FSS was 1 mm. The vibration information of the processed mirror was measured by changing the revolution frequency of the CCOS grinding system.

From the test results in Figure 24, it can be seen that, when the revolution frequency of the CCOS grinding system was 15, 25, and 50 Hz, the amplitude of the processed mirror significantly increased. This was related to the resonance of the first-order natural frequencies of the 5-DOF-HPR and the first-order natural frequencies of the FSS. In order to avoid the resonance of the machined mirror, the common speed of the CCOS grinding system should be adjusted according to the natural frequency of the FSS and the natural frequency of the 5-DOF-HPR to avoid the resonance of the machined mirror.

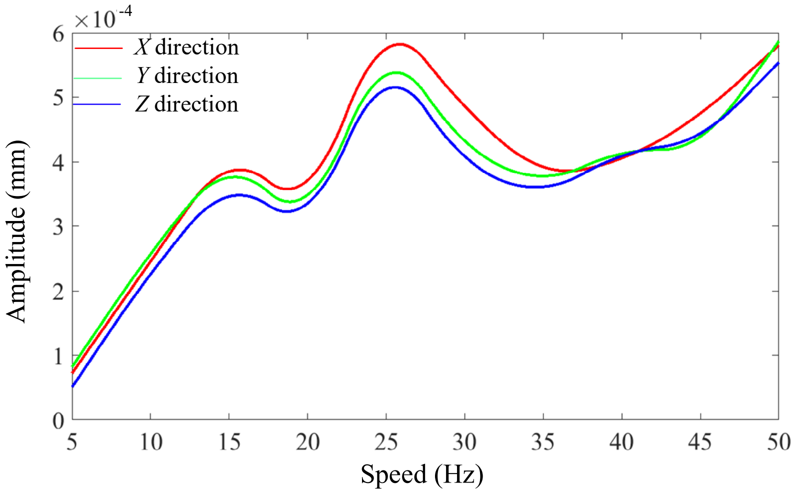

Figure 24. Amplitude of the CCOS grinding system at different speeds.

5. Conclusions

To improve the processing accuracy of the LOMPS, the perturbation relationship of the natural frequency of the robots to the processed, the mirror surface, and the vibration coupling between the robots were studied. The vibration differential equations of each robot were established and simulated. Then, it was verified through experiments that the error between the experimental natural frequency of the 5-DOF-HPR and the simulation result was within 12.5%, and the error between the experimental natural frequency and the simulation result of the FSS was less than 16%. Compared with the first four natural frequencies of the bottom support and mirror, the natural frequency of the bottom support increased. Thus, the validity and accuracy of the established mathematical model were verified, providing a basis for follow-up research on path planning and control systems of the LOMPS. Finally, the amplitude of the machined mirror under different speeds of the 5-DOF-HPR, different support heights of the FSS, and different rotational speeds of the CCOS grinding system were measured, and the vibration characteristics of the machined mirror under different influencing factors were analyzed. The experimental results showed that, when the revolution frequency of the CCOS grinding system was close to the natural frequency of the 5-DOF-HPR and the natural frequency of the FSS, the resonance phenomenon occurred, resulting in an increase in amplitude.

The proposed method provides a theoretical basis for analyzing the vibration characteristics of the LOMPS and improving the surface accuracy of the processed mirror. It also provides an experimental basis for research on the dynamic characteristics of a machining system composed of multiple heterogeneous robots, such as this machine–electro-hydraulic collaborative work. At the same time, it also demonstrates the feasibility of precision machining of multiconfiguration robots in complex disturbance environments.

Author Contributions: Conceptualization, Z.J.; methodology, Z.Y.; software, Z.J.; validation, Z.J. and F.L.; formal analysis, Z.J.; investigation, H.L.; resources, Z.J. and Z.Y.; data curation, H.L.; writing—original draft preparation, Z.J.; writing—review and editing, Z.Y.; visualization, H.L.; supervision, Z.Y.; project administration, Z.Y.; funding acquisition, Z.J., H.L. and Z.Y. All authors have read and agreed to the published version of the manuscript.

Funding: This research was funded by the Doctoral Scientific Research Foundation of Suzhou University, grant number 2023BSK016 (Z.J.); the Key Project of Natural Science Research in Universities of Anhui Province, grant number 2022AH051380 (Z.Y.), 2023AH052237 (H.L.), and 2024AH051812 (Z.J.); the Excellent Scientific Research and Innovation Teams in Anhui Province's Universities, grant number 2023AH010055 (Z.J., Z.Y.); the Key Research and Development Program Projects in Anhui Province, grant number 2023t070200 (Z.Y.); the Anhui Province Higher Education Provincial Quality Engineering Project, grant number 2023sdxx088 (Z.Y., Z.J.) and 2023cyts045 (Z.Y., Z.J.).

Data Availability Statement: Data are contained within the article.

Conflicts of Interest: Author Fuchao Liu was employed by the company Shandong Xinsha Monorail Transport Equipment Co., Ltd. The remaining authors declare that the research was conducted in the absence of any commercial or financial relationships that could be construed as a potential conflict of interest.

Abbreviations

CCOS	Computer-Controlled Optical Surfacing
5-DOF-HPR	Five-Degrees-of-Freedom Hybrid Processing Robot
FSS	Flexible Support System
LOMPS	Large Optical Mirror Processing System

References

1. Jin, Z.J.; Cheng, G.; Guo, F.; Chen, S.B. Human-machine-environment information fusion and control compensation strategy for large optical mirror processing system. *Proc. Inst. Mech. Eng. Part C-J. Eng. Mech. Eng. Sci.* **2020**, *35*, 2507–2523. [CrossRef]
2. Jiang, B.C.; Zhao, D.W.; Wang, B.Q.; Zhao, H.J.; Liu, Y.H.; Lu, X.C. Flatness maintenance and roughness reduction of silicon mirror in chemical mechanical polishing process. *Sci. China-Technol. Sci.* **2020**, *63*, 166–172. [CrossRef]
3. Kong, Y.X.; Cheng, G.; Guo, F.; Gu, W.; Zhang, L.B. Inertia matching analysis of a 5-DOF hybrid optical machining manipulator. *J. Mech. Sci. Technol.* **2019**, *33*, 4991–5002. [CrossRef]
4. Sun, T.; Lian, B.B.; Song, Y.M.; Feng, L. Elastodynamic optimization of a 5-DoF parallel kinematic machine considering parameter uncertainty. *IEEE-ASME Trans. Mechatron.* **2019**, *24*, 315–325. [CrossRef]
5. Lin, C.J.; Wang, H.C.; Wang, C.C. Automatic calibration of tool center point for six degree of freedom robot. *Actuators* **2023**, *12*, 107. [CrossRef]
6. He, F.X.; Dai, L.; Chen, Q.S.; Liu, Y.; Luo, Z. Three-dimensional stability analysis of robotic machining process. *Ind. Robot.-Int. J. Robot. Res. Appl.* **2020**, *47*, 82–89. [CrossRef]
7. Gierlak, P.; Warminski, J. Analysis of bifurcation vibrations of an industrial robot arm system with joints compliance. *Appl. Sci.* **2023**, *13*, 11941. [CrossRef]
8. Ariano, A.; Perna, V.; Senatore, A.; Scatigno, R.; Nicolo, F.; Fazioli, F.; Avallone, G.; Pesce, S.; Gagliano, A. Simulation and experimental validation of novel trajectory planning strategy to reduce vibrations and improve productivity of robotic manipulator. *Electronics* **2020**, *9*, 581. [CrossRef]
9. Hwang, S.W.; Bak, J.H.; Yoon, J.; Park, J.H. Oscillation Reduction and frequency analysis of under-constrained cable-driven parallel robot with three cables. *Robotica* **2020**, *38*, 375–395. [CrossRef]
10. Zhang, T.; Lin, K.Y.; Zhang, A.M. Research on flexible dynamics of a 6-DOF industrial robot and residual vibration control with a pre-adaptive input shaper. *J. Mech. Sci. Technol.* **2019**, *33*, 1875–1889. [CrossRef]
11. Min, F.Y.; Wang, G.; Liu, N. Collision detection and identification on robot manipulators based on vibration analysis. *Sensors* **2019**, *19*, 1080. [CrossRef] [PubMed]
12. Yoon, H.J.; Chung, S.Y.; Kang, H.S.; Hwang, M.J. Trapezoidal motion profile to suppress residual vibration of flexible object moved by robot. *Electronics* **2019**, *8*, 30. [CrossRef]
13. Wu, Y.; Yu, K.P.; Jiao, J.; Cao, D.Q.; Chi, W.C.; Tang, J. Dynamic isotropy design and analysis of a six-DOF active micro-vibration isolation manipulator on satellites. *Robot. Comput.-Integr. Manuf.* **2018**, *49*, 408–425.
14. Yang, H.Y.; Zhou, Z.G.; Dang, Y.G.; Wang, X.Y.; Li, G.G.; Xu, Z.D. Nonlinear dynamics characteristics of a magnetically actuated dual-spin capsule robot. *Nonlinear Dyn.* **2023**, *111*, 20771–20792. [CrossRef]

15. Tang, X.W.; Li, Z.P.; Yan, R.; Peng, F.Y.; Fan, Z. Operational impact excitation method for milling robot end frequency response function identification under movement state and pose-dependent dynamic compliance analysis. *J. Manuf. Sci. Eng.-Trans. ASME* **2023**, *145*, 034501. [CrossRef]
16. Hoevenaars, A.G.L.; Krut, S.; Herder, J.L. Jacobian-based natural frequency analysis of parallel manipulators. *Mech. Mach. Theory* **2020**, *148*, 103775. [CrossRef]
17. Ma, S.G.; Liang, B.; Wang, T.S. Dynamic analysis of a hyper-redundant space manipulator with a complex rope network. *Aerosp. Sci. Technol.* **2020**, *100*, 105768. [CrossRef]
18. Wu, J.J. Finite element analysis and vibration testing of a three-dimensional crane structure. *Measurement* **2006**, *39*, 740–749. [CrossRef]
19. Nguyen, V.; Cvitanic, T.; Melkote, S. Data-driven modeling of the modal properties of a six-degrees-of-freedom industrial robot and its application to robotic milling. *J. Manuf. Sci. Eng.-Trans. ASME* **2019**, *141*, 121006. [CrossRef]
20. Ganesh, S.S.; Rao, A.B.K. Design optimization of a 2-DOF parallel kinematic machine based on natural frequency. *J. Mech. Sci. Technol.* **2020**, *34*, 835–841. [CrossRef]
21. Dong, C.L.; Liu, H.T.; Huang, T.; Chetwynd, D.G. A screw theory-based semi-analytical approach for elastodynamics of the tricept robot. *J. Mech. Robot.-Trans. ASME* **2019**, *11*, 031005. [CrossRef]
22. Yang, Q.J.; Zhu, R.; Niu, Z.G.; Chen, C.; Mao, Q.; Zheng, Y.J. Natural frequency analysis of hydraulic quadruped robot and structural optimization of the leg. *J. Dyn. Syst. Meas. Control-Trans. ASME* **2020**, *142*, 011009. [CrossRef]
23. Li, J.; Wang, Y.; Zhang, K.; Wang, Z.Q.; Lu, J.X. Design and analysis of demolition robot arm based on finite element method. *Adv. Mech. Eng.* **2019**, *11*, 1–9. [CrossRef]
24. Guan, E.G.; Miao, H.H.; Li, P.B.; Liu, J.H.; Zhao, Y.Z. Dynamic model analysis of hydraulic support. *Adv. Mech. Eng.* **2019**, *11*, 168781401882014. [CrossRef]
25. Lin, Z.H.; Huang, Y.D. Effect of bell plate structure on high- and low-frequency characteristics of hydraulic mount. *Appl. Rheol.* **2024**, *34*, 20240014. [CrossRef]
26. Xie, B.W.; Yang, Y. Study on working characteristics of 4-column hydraulic support in lifting-lowering-moving state based on microcontact theory and rigid-flexible-mechanical-hydraulic coupling simulation model. *Actuators* **2024**, *13*, 193. [CrossRef]
27. Xu, H.G.; Zhang, J.H.; Sun, G.M.; Huang, W.D.; Huang, X.C.; Lyu, F.; Xu, B.; Su, Q. The direct measurement of the cylinder block dynamic characteristics based on a non-contact method in an axial piston pump. *Measurement* **2021**, *167*, 108279. [CrossRef]
28. Tao, M.L.; Lin, F.; Shu, L.; Deng, H.B.; Zhang, Y.H. Research on impedance network modeling and output characteristics of magnetostrictive electro-hydraulic actuator. *J. Adv. Mech. Des. Syst. Manuf.* **2023**, *17*, 2023. [CrossRef]